



Type I interferon transcriptional network regulates expression of coinhibitory receptors in human T cells

Tomokazu S. Sumida^{1,9}✉, Shai Dulberg^{2,9}, Jonas C. Schupp^{3,4,9}, Matthew R. Lincoln^{1,5}, Helen A. Stillwell¹, Pierre-Paul Axisa¹, Michela Comi¹, Avraham Unterman^{3,6}, Naftali Kaminski³, Asaf Madi^{1,2,7}✉, Vijay K. Kuchroo^{7,8} and David A. Hafler^{1,8}

Although inhibition of T cell coinhibitory receptors has revolutionized cancer therapy, the mechanisms governing their expression on human T cells have not been elucidated. In the present study, we show that type I interferon (IFN-I) regulates coinhibitory receptor expression on human T cells, inducing PD-1/TIM-3/LAG-3 while inhibiting TIGIT expression. High-temporal-resolution mRNA profiling of IFN-I responses established the dynamic regulatory networks uncovering three temporal transcriptional waves. Perturbation of key transcription factors (TFs) and TF footprint analysis revealed two regulator modules with different temporal kinetics that control expression of coinhibitory receptors and IFN-I response genes, with SP140 highlighted as one of the key regulators that differentiates LAG-3 and TIGIT expression. Finally, we found that the dynamic IFN-I response in vitro closely mirrored T cell features in acute SARS-CoV-2 infection. The identification of unique TFs controlling coinhibitory receptor expression under IFN-I response may provide targets for enhancement of immunotherapy in cancer, infectious diseases and autoimmunity.

Immune checkpoint blockade targeting T cell coinhibitory receptors has revolutionized cancer treatment. Although signals such as interleukin (IL)-27 are associated with T cell expression of coinhibitory receptors in mice^{1,2}, the regulatory mechanisms of coinhibitory receptor induction in human T cells are still unknown. IFN-I serves as a first-line defense system against viral infection, and its effect on T cells has been extensively studied in the context of T cell activation³, survival⁴ and effector functions⁵. IFN-I is also induced during chronic viral infection, autoimmunity and cancer^{6–8}, and accumulating evidence suggests that IFN-I may have immunomodulatory functions beyond their conventional role on T cells in acute viral infection^{9–12}. Notably, continuous exposure to IFN-I is implicated to promote T cell exhaustion, which is marked by aberrant expression of coinhibitory receptors (that is, programmed cell death protein 1 (PD-1), T cell immunoglobulin mucin-3 (TIM-3), lymphocyte activating 3 (LAG-3) and TIGIT (T cell immunoreceptor with immunoglobulin and ITIM domains)) in chronic viral infection and cancer^{12–16}. Although IFN-I has a central role in regulating immune responses and murine models have enabled the elucidation of a functional role of IFN-I on T cells, it has become clear that this response varies greatly between rodents and humans¹⁷. Thus, it is of critical importance to elucidate the biological consequences of IFN-I on human T cells and in the context of human diseases.

In the present study, we constructed a dynamic gene-regulatory network of human primary T cell response to IFN-I stimulation

using high-resolution gene expression profiling, chromatin accessibility analysis and perturbation of key network regulators. This regulatory network revealed both canonical and noncanonical IFN-I transcriptional regulators and identified unique regulators that control the expression of coinhibitory receptors. To provide direct in vivo evidence for the role of IFN-I on coinhibitory receptors, we then performed single-cell RNA-sequencing (scRNA-seq) in subjects infected with SARS-CoV-2, where viral load was strongly associated with T cell IFN-I signatures. We found that the dynamic IFN-I response in vitro closely mirrored T cell features with acute IFN-I-linked viral infection, with high *LAG3* and decreased *TIGIT* expression. Finally, our gene-regulatory network identified *SP140* as a key regulator for differential *LAG3* and *TIGIT* expression. The construction of coinhibitory regulatory networks induced by IFN-I and unique TFs controlling their expression provides further resources for the identification of targets for enhancement of immunotherapy in cancer, infectious diseases and autoimmunity.

Results

The impact of IFN- β on coinhibitory receptors in human T cells.

IL-27 has been identified as a crucial cytokine that promotes the induction of a coinhibitory receptor module, with T cell exhaustion in murine tumor models¹. Several reports have suggested that IL-27 functions downstream of IFN- β ¹⁸, an important member of the IFN-I family. Thus, we hypothesized that IFN- β facilitates the induction of coinhibitory receptors in humans. We first assessed

¹Departments of Neurology and Immunobiology, Yale School of Medicine, New Haven, CT, USA. ²Department of Pathology, Sackler School of Medicine, Tel Aviv University, Tel Aviv, Israel. ³Section of Pulmonary, Critical Care and Sleep Medicine Section, Department of Internal Medicine, Yale School of Medicine, New Haven, CT, USA. ⁴Department of Respiratory Medicine, Hannover Medical School and Biomedical Research in End-stage and Obstructive Lung Disease Hannover, German Lung Research Center, Hannover, Germany. ⁵Department of Medicine, Division of Neurology, University of Toronto, Toronto, Ontario, Canada. ⁶Pulmonary Institute, Tel Aviv Sourasky Medical Center, Tel Aviv University, Tel Aviv, Israel. ⁷Evergrande Center for Immunologic Diseases and Ann Romney Center for Neurologic Diseases, Harvard Medical School and Brigham and Women's Hospital, Boston, MA, USA.

⁸Broad Institute of MIT and Harvard, Cambridge, MA, USA. ⁹These authors contributed equally: Tomokazu S. Sumida, Shai Dulberg, Jonas C. Schupp.

✉e-mail: tomokazu.sumida@yale.edu; asafmadi@tauex.tau.ac.il

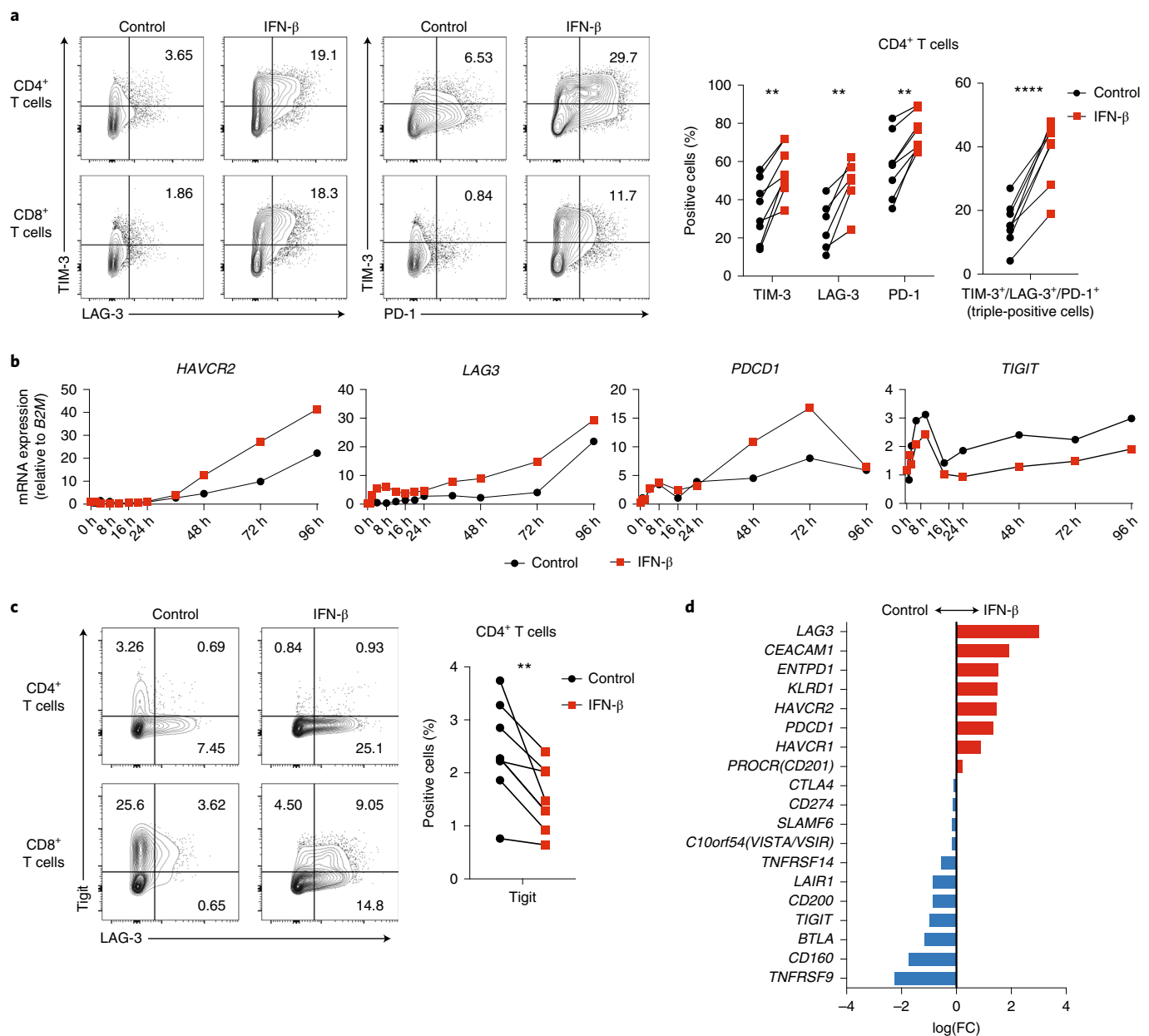


Fig. 1 | IFN-β regulates LAG-3, TIM-3, PD-1 and TIGIT differently in human T cells. Effects of IFN-β on LAG-3, TIM-3, PD-1 and TIGIT expression on human naive CD4⁺ and CD8⁺ T cells cultured with anti-CD3/CD28 for 96 h in the absence (Control) or with 500 U ml⁻¹ of IFN-β (IFN-β). **a**, Representative contour plots of flow cytometry analysis on surface LAG-3, TIM-3 and PD-1 (left), quantitative expression for LAG-3, TIM-3 and PD-1 expression on naive CD4⁺ T cells (*n* = 6 biologically independent samples) (middle) and quantitative analysis for triple-positive (LAG-3, TIM-3 and PD-1) cells in naive CD4⁺ T cells (*n* = 6 biologically independent samples) (right). **b**, Gene expression kinetics of *LAG3*, *HAVCR2*, *PDCD1* and *TIGIT* quantified by qPCR with 13 timepoints in naive CD4⁺ T cells. Average expression values from two subjects are plotted. **c**, IFN-β induces LAG-3 but suppresses TIGIT expression on human naive CD4⁺ and CD8⁺ T cells. Representative contour plots of flow cytometry analysis (left) and quantitative analysis for TIGIT positive cells in naive CD4⁺ T cells (*n* = 8 biologically independent samples) (right) are shown. **d**, Coinhibitory receptor expression pattern under IFN-β treatment in naive CD4⁺ T cells by qPCR (*n* = 4 biologically independent samples). Red and blue bars represent higher expression in IFN-β treatment and control conditions, respectively. Data were represented as mean ± s.d. ***P* < 0.01, *****P* < 0.0001, using a paired Student's *t*-test.

the effect of IL-27 and IFN-β on the induction of core coinhibitory receptors (TIM-3, LAG-3, PD-1 and TIGIT) in vitro using human primary naive CD4⁺ and CD8⁺ T cells (Extended Data Fig. 1). Both IL-27 and IFN-β promoted significantly higher TIM-3 expression compared with the expression of control groups without addition of exogenous cytokines. Of note, IFN-β induced more LAG-3 and TIM-3 expression compared with IL-27 in both CD4⁺ and CD8⁺ T cells (Fig. 1a and Extended Data Fig. 2a). Both IL-27 and IFN-β

suppressed the expression of TIGIT in CD4⁺ and CD8⁺ T cells (Extended Data Fig. 2b). We also observed increased production of IL-10 induced by IFN-β; however, IL-10 induction by IL-27 was modest in our in vitro culture settings, which may reflect the difference between mouse and human T cell responses toward IL-27 stimulation (Extended Data Fig. 2c). Next, we further determined the impact of IFN-β treatment on gene expression kinetics for coinhibitory receptors by quantitative (q)PCR. Gene expression dynamics

for core coinhibitory receptors (*HAVCR2*, *LAG3* and *PDCD1*) were upregulated by IFN- β for most timepoints. In contrast, *TIGIT* was downregulated, which was confirmed by protein expression using flow cytometry (Fig. 1b,c). We examined the expression of other coinhibitory receptors and found that IFN- β induced coexpression of multiple coinhibitory receptors (for example, *HAVCR2*, *PDCD1* and *LAG3*) but inhibited expression of others (for example, *TIGIT*, *CD160* and *BTLA*) (Fig. 1d and Extended Data Fig. 2d). As T cell activation and entry into the cell cycle could be confounding factors for the measurement of coinhibitory receptor expression, we performed proliferation assays using CellTrace Violet dye and examined the level of T cell activation markers (CD25, CD44 and CD69) with IFN- β treatment. There was no statistical difference in cellular division or degree of T cell activation between control and the IFN- β condition after 4 d of human primary T cell culture. In addition, there was even less proliferation of memory CD4⁺ T cells with IFN- β , indicating that the induction of coinhibitory receptors by IFN- β is not affected by T cell activation state (Extended Data Fig. 3a–c), consistent with previous studies^{19,20}. Furthermore, we confirmed a dose-dependent effect of IFN- β treatment on coinhibitory receptor expressions (Extended Data Fig. 3d). The effects of IFN- β on the level of LAG-3, TIM-3, PD-1 and TIGIT were consistently observed across each cellular division status, strongly suggesting that IFN- β -induced changes on coinhibitory receptors were not biased by T cell proliferation (Extended Data Fig. 3e). Collectively, these data elucidate a role for IFN- β as a cytokine that can directly control multiple coinhibitory receptors in both human CD4⁺ and CD8⁺ T cells in vitro.

High-resolution transcriptomic dynamics of IFN- β response. To uncover the regulatory mechanisms underlying the IFN- β response in human primary T cells, we generated a transcriptional profile at high temporal resolution. We used bulk messenger (m)RNA-seq at ten timepoints along a 96-h time course with and without IFN- β treatment (Extended Data Fig. 4a). To avoid interindividual genetic variation, we selected one healthy subject whose T cells exhibited a stable response to IFN- β , and repeated the experiment three times at a 2-week interval for each experiment, analogous to studying one mouse strain. We identified 1,831 differentially expressed genes (DEGs) for CD4⁺ T cells and 1,571 DEGs for CD8⁺ T cells across timepoints with IFN- β treatment, revealing a temporal shift of gene expression patterns in both CD4⁺ and CD8⁺ T cells (Fig. 2a, Extended Data Fig. 4b and Methods). The genome-wide transcriptional profiles from three independent experiments demonstrated highly consistent results across timepoints (Fig. 2b). Specifically, three transcriptional waves were observed during 96 h of IFN- β response: early phase (1–2 h), intermediate phase (4–16 h) and late phase (48–96 h). As expected, we observed abundant induction of classic IFN-stimulated genes (ISGs) (that is, *IFI6*, *MX1/2*, *RSAD2*, *STAT1/2/3* and *SP100/110/140*), which peaked at the early intermediate phase. IFN-I-induced cytokines produced by T cells (*IFNG*, *IL10*, *GZMB* and *PRF1*) were also upregulated at intermediate-late phase (Fig. 2c and Extended Data Fig. 4c). *OSM* (oncostatin M), which is reported to amplify IFN- β response and suppress differentiation of helper T cells (T_H17)²⁰, was significantly induced by IFN- β from the early phase and maintained induction at all timepoints (Extended Data Fig. 4c). Among DEGs, we identified

dynamic expression of 134 TFs for CD4⁺ T cells and 100 TFs for CD8⁺ T cells, which were both up- and downregulated over the course of differentiation (Fig. 2c). We further explored the dynamic changes at the level of chromatin accessibility by using an assay for transposase-accessible chromatin sequencing (ATAC-seq)²¹ for CD4⁺ and CD8⁺ T cells over three different timepoints corresponding to three transcriptional waves (2, 8 and 72 h) (Extended Data Fig. 5a). Principal component analysis (PCA) highlighted the differential chromatin accessibility at the late phase (72 h) compared with the other phases (Extended Data Fig. 5b). Differential chromatin accessibility analysis at each timepoint identified temporal changes of chromatin accessibility; in the control, the chromatin accessibility was reduced at the early timepoint (2 h) and then became more accessible over time (Extended Data Fig. 5c). This temporal change was altered by IFN- β treatment with more chromatin accessibility compared with the control condition at 8 h, which was further enhanced at 72 h (Extended Data Fig. 5d). Taken together, these high-temporal-resolution transcriptional and chromatin accessibility data highlight the impact of IFN- β treatment on both the dynamics of T cell activation and their final differentiation state.

Genetic perturbation identifies two IFN-I regulatory modules. Genetic perturbation of key TFs allows inference of the gene-regulatory network with our high-temporal-resolution transcriptional data, leading to the elucidation of the regulatory mechanisms by which IFN-I response controls coinhibitory receptor expressions. To narrow the list of TFs for perturbation, we prioritized TFs that are differentially expressed in both CD4⁺ and CD8⁺ T cells. We then further selected TFs associated with T cell exhaustion: (1) human tumor-infiltrating T cells (TILs)^{22–25}; (2) HIV-specific T cell signature in progressive patients²⁶; and (3) IL-27-driven coinhibitory regulators¹ (Methods). We confirmed that these TFs are identified as ISGs in human immune cells by the Interferome dataset²⁷ (Fig. 3a). In total, 31 TFs were listed as candidates based on the overlap of ISG, TIL and IL-27 signatures, and we chose 19 of them for perturbation. As TCF-1 (encoded by *TCF7*) and Blimp-1 (encoded by *PRDM1*) are known to express functionally distinct isoforms, we also targeted a unique sequence for the long isoforms (*TCF7L* and *PRDM1L*, respectively), resulting in perturbation of 21 different targets in total.

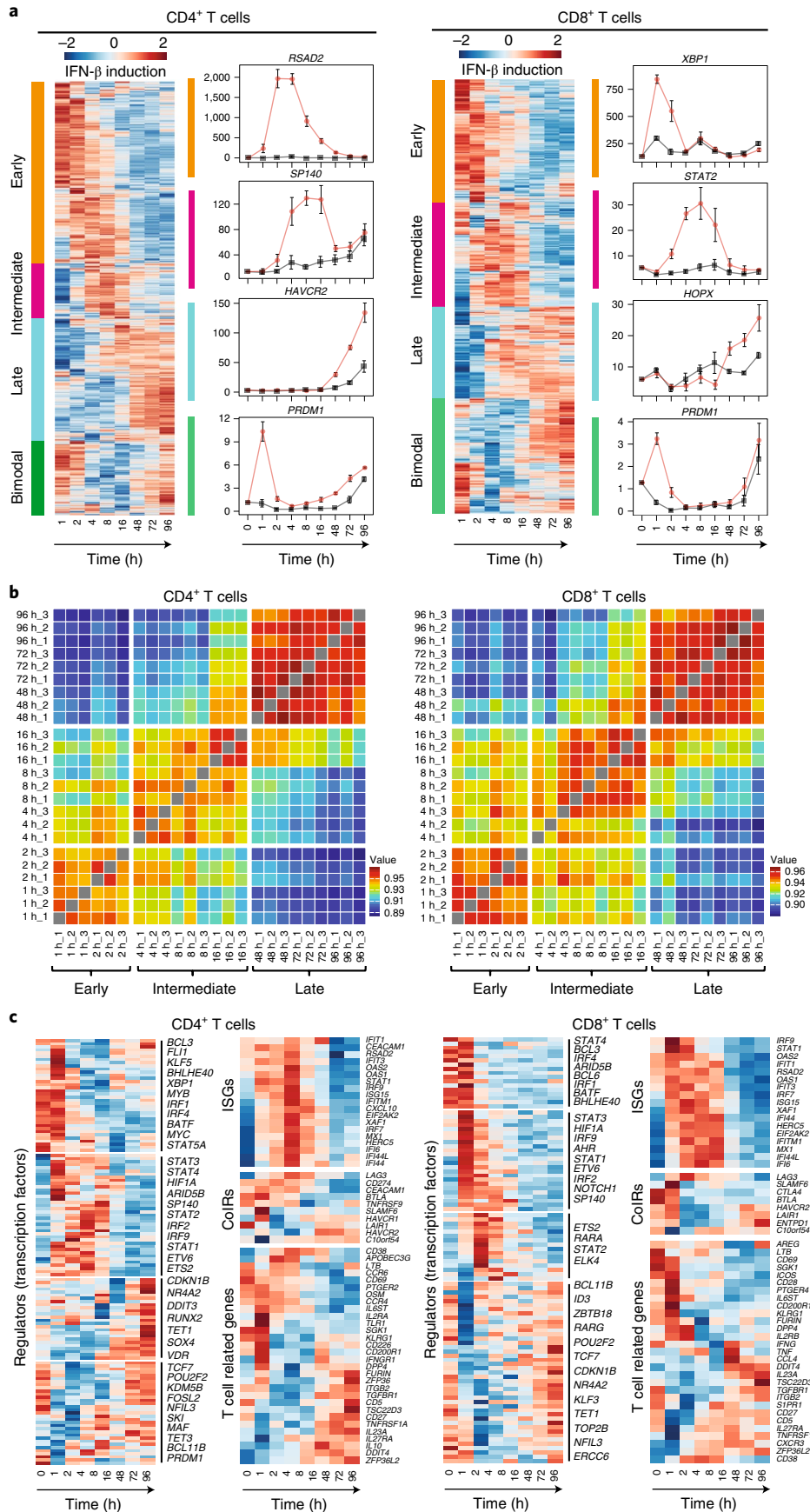
Considering that most of these regulators are induced at the early (1–2 h) and intermediate (4–16 h) phases, it was important to perform gene deletion before T cell receptor activation. For human primary T cell gene knockdown, we adopted lentiviral delivery of short hairpin (sh)RNAs with lentiviral gene product X (Vpx) containing virus-like particles (VLPs) to efficiently transduce lentivirus into unstimulated primary human naive T cells^{28,29} (Fig. 3b). Spinoculation with Vpx-VLPs increased the number of green fluorescent protein (GFP)-expressing T cells (~30–60%) compared with normal lentiviral particle transduction without Vpx-VLPs (~1–5%) and resulted in successful transduction of lentiviral vectors into nonblasting/quiescent cells (Extended Data Fig. 6a). We achieved efficient knockdown of at least 60% gene expression for 21 target TFs in human naive CD4⁺ T cells (Fig. 3c).

To identify the effect of perturbation for each regulator, PCA was applied to determine the changes in RNA expression associated with each TF knockdown (Fig. 3d). Principal component 1 (PC1)

Fig. 2 | Three waves of dynamic transcriptomic changes by IFN- β in human T cells. **a**, Gene expression profiles under IFN- β treatment in naive CD4⁺ and CD8⁺ T cells. Differential expression of gene levels for eight timepoints with IFN- β stimulation ($\log_2(\text{expression})$) are shown in the heatmap. Based on the expression kinetics, the genes are clustered into four categories: early, intermediate, late and bimodal (upregulated at early and late phases). Representative individual gene expression kinetics from each cluster are shown (mean \pm s.d.). **b**, Correlation matrix of global gene expression representing three transcriptional waves on CD4⁺ (left) and CD8⁺ T cells: early (1–2 h), intermediate (4–16 h) and late (48–96 h). Eight timepoints with three replicates are shown. **c**, Temporal transcriptional profiles of DEGs for four categories are shown: transcriptional regulators (TFs), ISGs, coinhibitory receptors and key T cell-associated factors for CD4⁺ (left) and CD8⁺ T cells.

divided the impact of perturbation into two modules of regulators: *BATF*, *MAF*, *ETS2*, *HOPX*, *SP140*, *BCL3*, *ID3* and *BATF3* constituted 'IFN- β regulator module 1', and *IRF1*, *IRF2*, *IRF4*, *STAT1*,

STAT3, *ARID5A*, *ARID5B*, *TCF7*, *PRDM1*, *PRDM1L*, *KLF5* and *TCF7L* constituted a distinct 'IFN- β regulator module 2'. To visualize the contribution of the selected genes to the PCs and the



directionality of the contribution, a PCA biplot analysis was adopted. In these biplots, the loadings of each variable (gene) are represented as arrows and the changes of gene expression by perturbation are represented as points, providing a faithful representation of the relationships for each gene (arrows) based on the contribution to the effect of each perturbation. We found that ISGs are divided into two groups: classic ISGs that are correlated with 'IFN-I regulator module 1' (depicted by orange arrows in Fig. 3e) and the other ISGs that are correlated with 'IFN-I regulator module 2' (depicted by green arrows in Fig. 3e; Extended Data Fig. 6b), which is predominantly explained by PC1. These results suggest that ISGs are bidirectionally regulated by different modules of TFs. Furthermore, these modules contributed differently to the regulation of coinhibitory receptors: *TIGIT*, *CD160* and *BTLA* as one module and *LAG3*, *HAVCR2* and *PDCD1* as another module (Fig. 3f and Extended Data Fig. 6c). Within 'IFN-I regulator module 1', *STAT3* positively regulated *HAVCR2* but not *LAG3* and *PDCD1* expression, which is predominantly contributed by PC2 in the biplot (Fig. 3f). Taken together, our perturbation with the Vpx-VLP system elucidated two distinct TF modules simultaneously regulating opposing IFN-I target genes, which sheds light on the central roles of noncanonical IFN-I induced regulators in human T cells.

Given that mRNA expression of TFs is not necessarily linked with the regulatory function of TFs, we performed footprint analysis on our ATAC-seq data using TOBIAS³⁰. IFN- β treatment enhanced the enrichment of interferon regulatory factor (IRF) and STAT (for signal transducers and activators of transcription) footprints at the early and intermediate phases; in contrast, AP-1 footprints were highly enriched at the late phase by IFN- β (Extended Data Fig. 6d). This dynamic switch of TF footprints from IRFs/STATs to the AP-1 family under IFN-I response represents the two differential regulatory modules indicated as IFN-I regulator module 1 (containing IRF1/2/4/9 and STAT1-3) and IFN-I regulator module 2 (containing AP-1 family TFs: BATF and BATF3) (Fig. 3g,h). In light of the role of AP-1 facilitating human T cell exhaustion with higher PD-1 and LAG-3 expression³¹, the enhanced AP-1 footprints at the later phase of IFN- β treatment support the role of IFN-I on induction of T cell exhaustion in human T cells^{11,12}. Taken together, the perturbation of key regulatory factors with an ATAC-seq footprint analysis revealed two different regulator modules that have different temporal characteristics of activation and differentially control ISGs and coinhibitory receptors under IFN-I response.

Dynamic regulatory network reveals central IFN-I regulators.

To characterize the impact of differentially expressed TFs (DETFs) in response to IFN- β , we generated transcriptional regulatory networks describing TFs and their target genes for each of the transcriptional waves identified (Fig. 4a and Methods). When comparing the three regulatory networks, early and late networks had similar numbers of TFs (46 and 42 TFs, respectively), although the intermediate network contained 73 TFs (Fig. 4b, top). The ratio between

up- and downregulated TFs differs across the three regulatory waves. The early and intermediate networks contained more upregulated than downregulated TFs; in contrast, the late network had more downregulated than upregulated TFs. Thus, IFN-I-induced differentiation involves dominance of upregulated TFs in the first 16 h, replaced by the dominance of downregulated TFs after 48 h. We next ranked the TFs based on the enrichment of their target genes and their centrality in the networks (Methods), highlighting the significance of each TF to the network (Fig. 4b, bottom). *STAT1/2*, which is well established as being directly downstream of IFN-I signaling, was highlighted as one of the top ranked upregulators in the early and intermediate-wave networks (Fig. 4b and Extended Data Fig. 4c). Of note, *STAT1* and *STAT2* showed contrastive scores with hypergeometric (HG) test and centrality (Cent)³²; *STAT1* was higher in Cent and lower in HG scores. In contrast, *STAT2* was higher in HG and lower in Cent scores. These data suggest that *STAT2* is specialized to control IFN-I regulatory TFs at early and intermediate phases, whereas *STAT1* is less specific to IFN-I signaling, but plays a more general role in T cell survival and memory formation^{26,33}. In the late network, effector function-related regulators were upregulated (*TBX21*, *HIF1A*, *FOSL1/2* and *MAF*); in contrast, the TFs associated with regulatory T cell (T_{reg} cell) differentiation and maintenance (*IKZF2*, *MYB*, *FOXP1* and *STAT5A*) were downregulated, suggesting the skewed differentiation toward an effector-like signature.

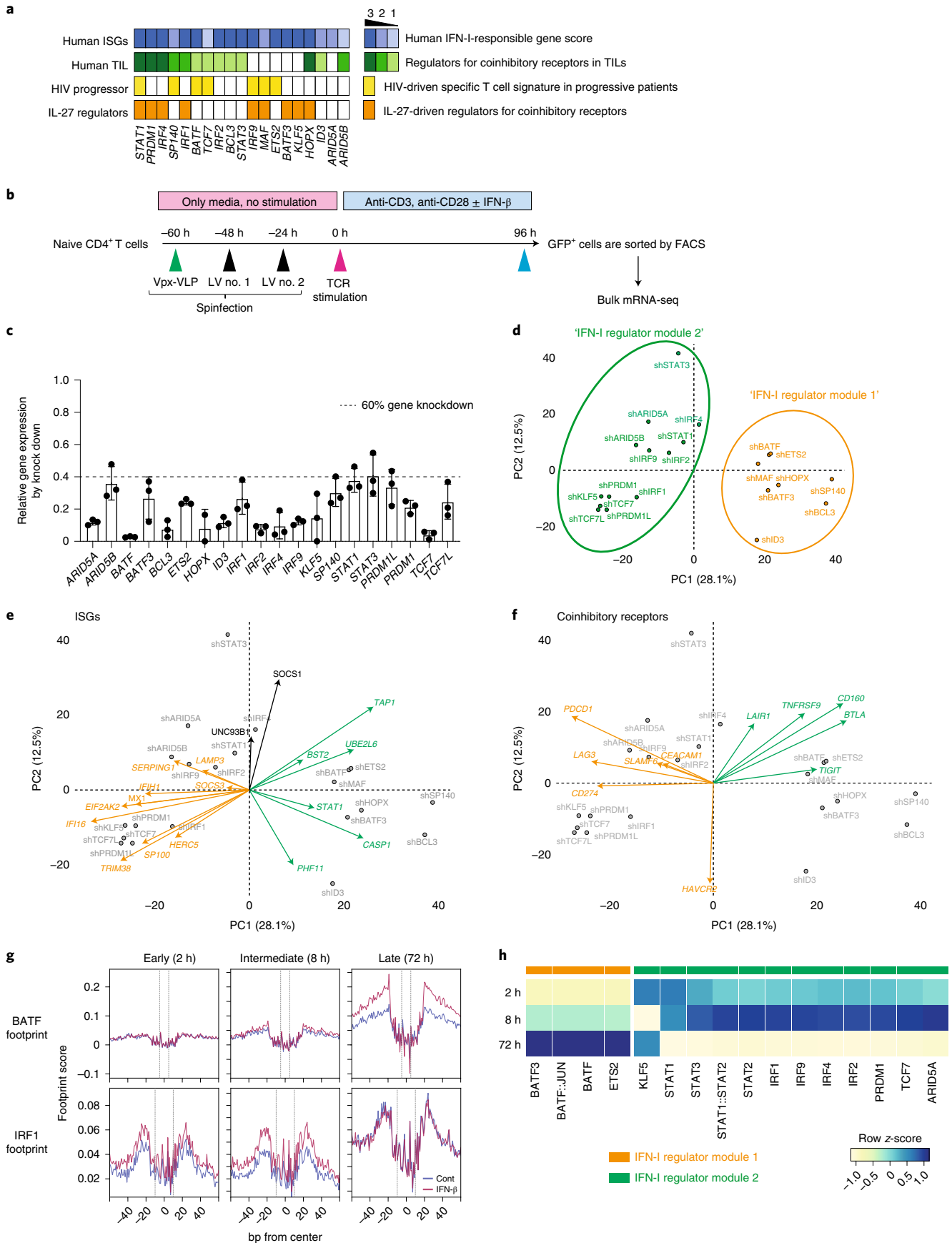
To further study the relationships between these IFN-I driven transcriptional regulators, we generated directed backbone networks that displayed the TFs that participate in each transcriptional time wave and visualized the interactions among them using the ECOplusMaST algorithm³² (Fig. 4c, Extended Data Fig. 7a and Methods). This analysis emphasizes that much of the signaling involves crossregulation between the TFs themselves. The central regulatory TFs, which are represented as more connected with the other TFs, were dominated by downregulated TFs in response to IFN- β (Fig. 4d) in all temporal transcriptional networks. In contrast, TFs less central were primarily upregulated. It is interesting that we found transforming growth factor β (TGF- β)-associated TFs (that is, *SKI*, *SMAD3* and *IKZF2*) and gene signatures enriched in the downregulated genes at each time wave (Fig. 4b, bottom heatmap, and Extended Data Fig. 7b), indicating counterregulatory mechanisms between IFN-I response and TGF- β signaling in human T cells^{34,35}. These results suggest that a loss of suppression by the key TFs that configure the backbone network may trigger the activation of downstream effector TFs under IFN-I response.

Although T cell differentiation under IFN- β is characterized by three major transcriptional waves, we hypothesized that there are key TFs that bridge each wave to the next. To this end, we specifically identified TFs that participate in more than one of these transcriptional waves, and termed these 'bridging TFs' (Fig. 4e). Examples of dominant bridging TFs between early and intermediate waves include *KLF5* and *STAT2*. Examples of intermediate-to-late

Fig. 3 | Perturbation of key TFs in quiescent human T cells. **a**, Characterization of candidate TFs for perturbation. Perturbed TFs are listed based on the overlap between DETFs of CD4⁺ T cells and CD8⁺ T cells. Human ISG score (top; blue), human TIL coinhibitory receptor score (green), HIV-specific T cell signature genes in progressive patients (yellow) and IL-27-driven coinhibitory receptor regulators (orange) are shown for each TF. **b**, Experimental workflow of Vpx-VLP-supported lentiviral shRNA perturbation. Ex vivo isolated naive CD4 T cells were transduced with Vpx-VLPs, followed by two lots of lentiviral particle transduction before starting T cell activation. T cells were stimulated with anti-CD3/CD28 in the absence or presence of IFN- β (500 U ml⁻¹) for 96 h and GFP-positive cells were sorted by FACS. RNAs were extracted from sorted cells and applied for mRNA-seq. Perturbations for all 21 shRNAs are performed with human CD4⁺ T cells isolated from the same individual as in Fig. 2. **c**, Gene knockdown efficiency is shown as relative expression over scrambled shRNA-transduced controls. The dotted line represents 60% of gene knockdown. **d-f**, PCA plots and biplots based on DEGs by perturbation. **d**, PCA plot demonstrating the two modules of TF regulators on perturbation with 21 TFs. Characterization of shRNA-based gene knockdown for each TF is plotted. Labels represent perturbed TF gene names. 'IFN-I regulator module 1' is colored green and 'IFN-I regulator module 2' is orange. **e,f**, PCA biplot showing differential regulation by modules of regulator TFs: for ISGs (**e**) and coinhibitory receptors (**f**). Orange and green arrows (vectors) highlight two groups of genes affected inversely by the different modules of TFs. **g**, Footprint plots for BATF and IRF1 at three timepoints (2, 8, 72 h). The dashed lines represent the edges of each TF motif. **h**, A heatmap showing the TF footprint activity of perturbed TFs across three phases.

waves include *MAF*, *PRDM1* and *MYB*. Finally, there are TFs that were upregulated throughout the entire differentiation, such as *STAT1*, *HIF1A* and *TBX21*. In general, bridging TFs tend to be

more dominant than other TFs; thus, it is possible that bridging TFs play an important role in the transition between different transcriptional waves. Indeed, our perturbation experiment demonstrated



the critical roles of those bridging TFs in the regulation of ISGs and coinhibitory receptors (Fig. 4e). Our computational analysis revealed the temporal dynamics of complex regulatory interactions during the IFN-I response and highlighted the usefulness of our approach in discovering this new aspect of IFN-I-induced transcriptional regulation.

In vivo link of IFN-I regulators and coinhibitory receptors.

To provide direct in vivo evidence for the role of IFN-I on T cell coinhibitory receptor expression, we sought to validate our regulatory network in humans where the IFN-I response of T cells is induced acutely. As acute viral infections are strongly associated with IFN-I responses, we examined a number of clinical models in which viral infection is closely linked to IFN-I T cell response. Our analysis of scRNA-seq data of T cells in COVID-19 patients revealed an extremely high correlation between viral load and IFN-I score ($r=0.8$), and a time difference between paired samples and the respective change in IFN-I score ($r=0.97$)³⁶, providing a unique opportunity to generate a rich dataset to determine whether the in vitro T cell response to IFN-I can be validated during an acute viral human infection strongly associated with a IFN-I signal.

By using our scRNA-seq data, we subclustered T cell populations into 13 subpopulations and identified 5 CD4⁺ T cell and 5 CD8⁺ T cell subsets (Fig. 5a and Extended Data Fig. 8a,b). We first focused on total CD4⁺ T cells and CD8⁺ T cells and confirmed that the IFN-I response signature is higher in progressive patients who required admission to the intensive care unit and eventually succumbed to the disease (Fig. 5b). Expression of coinhibitory receptors differed across disease conditions, but the trend was conserved between CD4⁺ and CD8⁺ T cells. We observed a strikingly similar pattern of coinhibitory receptor expression with IFN-I stimulation in vitro and in vivo. Indeed, we observed the upregulation of IFN-I up coinhibitory receptors (*LAG3/HAVCR2*) and the downregulation of IFN-I down coinhibitory receptors (*TIGIT/LAIR1/SLAMF6*) in T cells from COVID-19 patients (Figure 5c,d). As expected, IFN-I-up coinhibitory receptors were positively correlated with expression of canonical ISGs, but IFN-I-down coinhibitory receptors were not, suggesting that different regulatory mechanisms are dictating coinhibitory receptor expression patterns (Fig. 5e). Next, we investigated which subpopulation of CD4⁺ and CD8⁺ T cells is more affected by the IFN-I response and computed the IFN-I score across subpopulations for each T cell subtype in COVID-19 patients (Fig. 5f). Within the subpopulations that exhibited higher IFN-I scores, dividing CD4⁺/CD8⁺ T cells and ISG⁺CD8⁺ T cells were increased in COVID-19 patients, particularly in patients with severe disease^{36,37}. Moreover, these subpopulations and effector T cells expressed a higher level of coinhibitory receptors compared with the other subpopulations (Fig. 6a and Extended Data Fig. 8c). Of note, the IFN-I regulator module-1 score was higher in these T cell subsets than the IFN-I

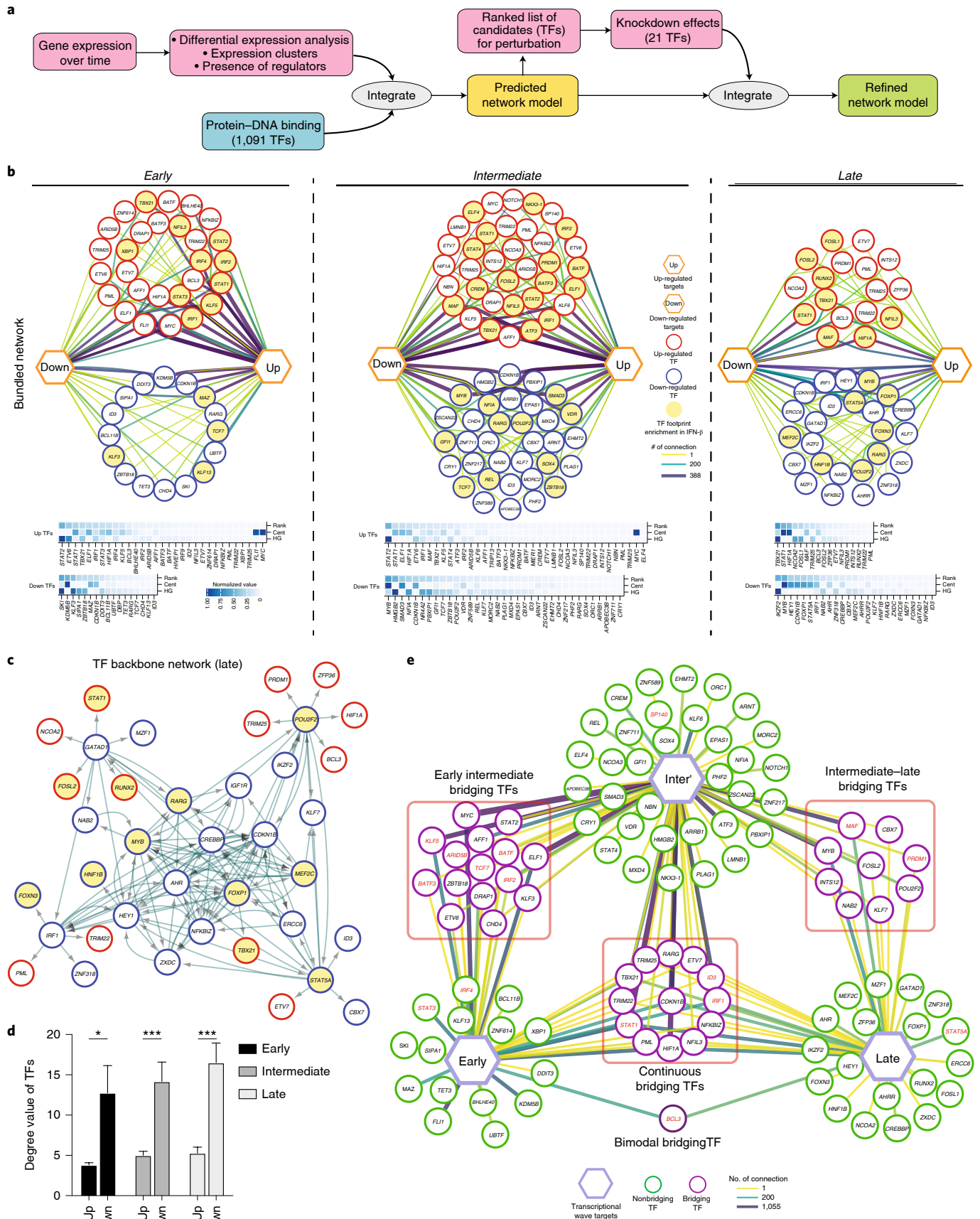
regulator module-2 score (Extended Data Fig. 8d), implying a more profound role of IFN-I regulator module 1 on controlling T cell signature in COVID-19.

We then examined which subpopulations were more enriched in the three transcriptional waves of IFN-I response. DEGs specific for each wave were used to compute the scores for the CD4⁺ and CD8⁺ T cell subpopulations in COVID-19 patients (Supplementary Table 1 and Methods). We found that T cells induced in vitro with IFN-I strongly mirrored the intermediate-wave score on dividing CD4⁺ and CD8⁺ T cells, and the late wave score on effector CD4⁺ T cells and ISG⁺CD8⁺/effector CD8⁺ T cells (Fig. 6b) in COVID-19 patients. Given that expansion of dividing CD4⁺/CD8⁺ T cells are a unique characteristic of acute viral infections, including COVID-19, we applied the intermediate phase IFN-I regulatory network with the dividing CD4⁺ T cell gene expression signature to examine the relationships between regulators and target genes in this subpopulation. This analysis highlights the regulators that function in establishing the characteristics of the dividing CD4⁺ T cell population under IFN-I response in vivo (Extended Data Fig. 8e). As *LAG-3* is the most upregulated coinhibitory receptor in the dividing CD4⁺ T cell population, we utilized the network analysis to elucidate the specific regulation of *LAG3* and *TIGIT* that were regulated in an opposing manner under IFN-I response both in vivo (Fig. 5c,d) and in vitro (Fig. 1). Analysis of the intermediate-wave, gene-regulatory network demonstrated that *SP140* is a bidirectional regulator for *LAG3* and *TIGIT* under IFN-I response, which is supported by the observation in COVID-19 patients, where increased *SP140* and *LAG3* but decreased *TIGIT* expression were demonstrated (Figs. 5c,d and 6c,d and Extended Data Fig. 8c). In addition, the late wave network demonstrated the complex interaction of regulators for *LAG3*, *HAVCR2* and *PDCD1*, in which *BCL3* and *STAT3* are highlighted as positive regulators on *LAG3* and *HAVCR2*, respectively (Fig. 6c). Importantly, both *BCL3* and *STAT3* were significantly elevated in T cells in COVID-19 patients (Fig. 6d). This can be highly relevant to effector T cell development under acute viral infection in which these coinhibitory receptors play a critical role in regulating effector function³⁸ and, of note, the late wave signature was enriched in effector T cells in COVID-19 patients (Fig. 6b). Finally, we validated the actions of these key regulators on major coinhibitory receptor expressions (*LAG-3*, *PD-1*, *TIM-3* and *TIGIT*) at the protein level with our in vitro system, where T cell proliferation was further controlled by determining T cell division state in parallel with gene knockdown (Extended Data Fig. 9a,b). In addition, *STAT5A* overexpression suppressed *PD-1* induction under IFN- β treatment in human primary CD4⁺ T cells, which validated the observation that *STAT5A* negatively regulates coinhibitory receptors, and its downregulation is necessary to elicit IFN-I-mediated *PD-1* expression (Fig. 6e and Extended Data Fig. 9c). We also confirmed that T cell activation was not significantly altered by gene perturbation across conditions (Extended

Fig. 4 | Transcriptional regulatory network under IFN-I response. **a**, Overview of regulatory network generation. **b**, In-depth view of the transcriptional regulation at each transcriptional wave. Top row: representation of regulatory networks highlighting TF interaction. The thicker and darker an edge is the more TF-target connections it represents. Target genes are represented by up and down hexagons, according to their response to IFN- β . Middle row: heatmaps representing a ranking of the TFs based on their centrality, connectivity and gene-target enrichment in the corresponding regulatory network. 'Cent' stands for centrality, which is a parameter that is given to each node, based on the shortest path from the node to the other nodes in the network. It represents how central and connected a node is to the rest of the network. 'HG' stands for hypergeometric; the value in the heatmap is the $-\log_{10}(P \text{ value})$ of an HG enrichment test of target genes of each TF in the network. The rank column is an average of both HG and Cent values, after score rescaling (0-1). **c**, Directed TF backbone networks at the late wave. The regulation and interaction of each DETF at each transcriptional wave were depicted. **b,c**, Red circles represent upregulated TFs and blue circles downregulated TFs, and the arrows represent the direction of regulation from TF to TF. TF footprints enriched in IFN- β condition were highlighted in yellow. **d**, Barplot showing the mean level of the degree of connectivity values for either up- or downregulated DETFs. The P values were calculated using an independent, two-way Student's t -test. * $P < 0.05$, *** $P < 0.001$. **e**, Dynamics of TFs regulation across the transcriptional waves. Each hexagon represents targets from each transcriptional wave. Green circles represent regulatory TFs that are differentially expressed only in one transcriptional wave to which they are connected, whereas purple circles represent bridging TFs, which are differentially expressed in all transcriptional waves to which they are connected. Perturbed TFs in Fig. 3 were highlighted in red. The thicker and darker an edge is, the more TF-target connections it represents.

Data Fig. 9d), suggesting that our in vitro perturbation system with shRNA-mediated gene knockdown was not confounded by T cell activation or proliferation, two well-known factors linked with

coinhibitory receptor expression. Taken together, these findings strongly suggest that in vitro regulatory networks can be utilized as a powerful tool to explore the human acute viral response in vivo.



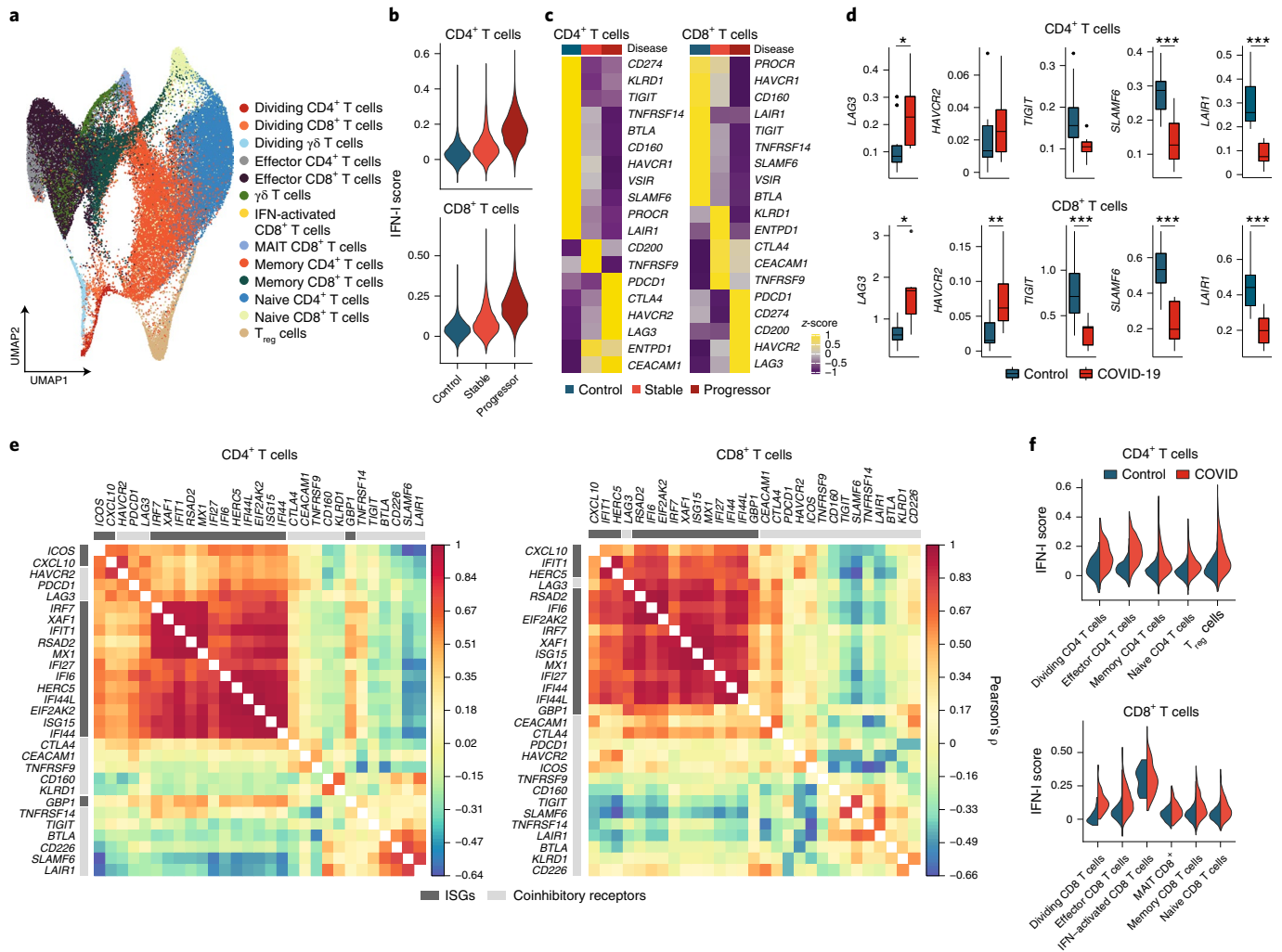


Fig. 5 | Linked IFN-I response and coinhibitory receptor expression in T cells in COVID-19. a, UMAP representation of T cells from healthy control samples ($n=13$ biologically independent samples) and COVID-19 samples ($n=18$ biologically independent samples). Thirteen subclusters were identified. **b**, IFN-I score for CD4⁺ and CD8⁺ T cells across the three disease conditions. **c**, Heatmaps for coinhibitory receptor expression in CD4⁺ and CD8⁺ T cells across the three disease conditions. **d**, Expression of key coinhibitory receptors between control and COVID-19 for CD4⁺ and CD8⁺ T cells. Average expression per subject for each gene is shown. * $P < 0.05$, ** $P < 0.01$, *** $P < 0.001$, using a two-sided Kruskal-Wallis test. **e**, Correlation matrix of ISGs (dark gray) and coinhibitory receptors (light gray) in CD4⁺ and CD8⁺ T cells in COVID-19 patients. **f**, IFN-I score for subsets of CD4⁺ and CD8⁺ T cells between control and COVID-19.

Discussion

In the present study, our systematic, computational and biological approach identifies IFN-I as a major driver of coinhibitory receptor regulation in human T cells. Although classic ISG induction has been extensively studied, those investigations have focused primarily on the canonical JAK-STAT pathway downstream of IFN-I receptor. Given that IFN-I exhibits multiple functions in context-dependent roles, a more complex understanding of the IFN-I response beyond this canonical pathway with a more extensive analysis of ISG transcriptional regulation in T cells is critical for elucidating the mechanism of coinhibitory receptor regulation.

In the present study, we comprehensively explored the induction of coinhibitory receptor expression with IFN-I, elucidating previously unrecognized patterns of T cell coinhibitory receptors. Although previous studies have shown that PD-1 is induced by IFN-I in T cells using mouse models of viral infection³⁹ and the blockade of IFN-I restores T cell effector capacity with reduction of PD-1 and TIM-3 in the chronic HIV infection model¹⁶, the full spectrum of coinhibitory receptor expression controlled by IFN-I in the context

of human diseases has not been investigated. In the present study, we build a dynamic gene-regulatory network that controls IFN-I response and identify key regulatory modules of ISG transcription in T cell responses to IFN- β . Our approach revealed two mutually antagonistic modules of ISG regulators, which exhibit opposite temporal kinetics under IFN- β treatment and may explain how the harmonized IFN-I-induced T cell response is achieved. Within the two modules, we highlighted SP140 as a potential regulator that controls LAG-3 and TIGIT in an opposing manner, and STAT3 as a positive regulator for TIM-3. SP140 might have a DNA-binding motif similar to AP-1 (ref. 40), which supports our findings of SP140 as one of the IFN-I regulatory module 1 TFs that contains AP-1 family TFs. These findings provide new insight into the landscape of the ISG transcriptional network and shed light on the large contribution of the noncanonical IFN-I pathway during IFN-I response in T cells^{37,41,42}. Although the newly identified regulators (for example, SP140 and BCL3) in the present study are not necessarily directly downstream of the conventional JAK/STAT pathway and may act differently depending on the context, they are nevertheless attractive

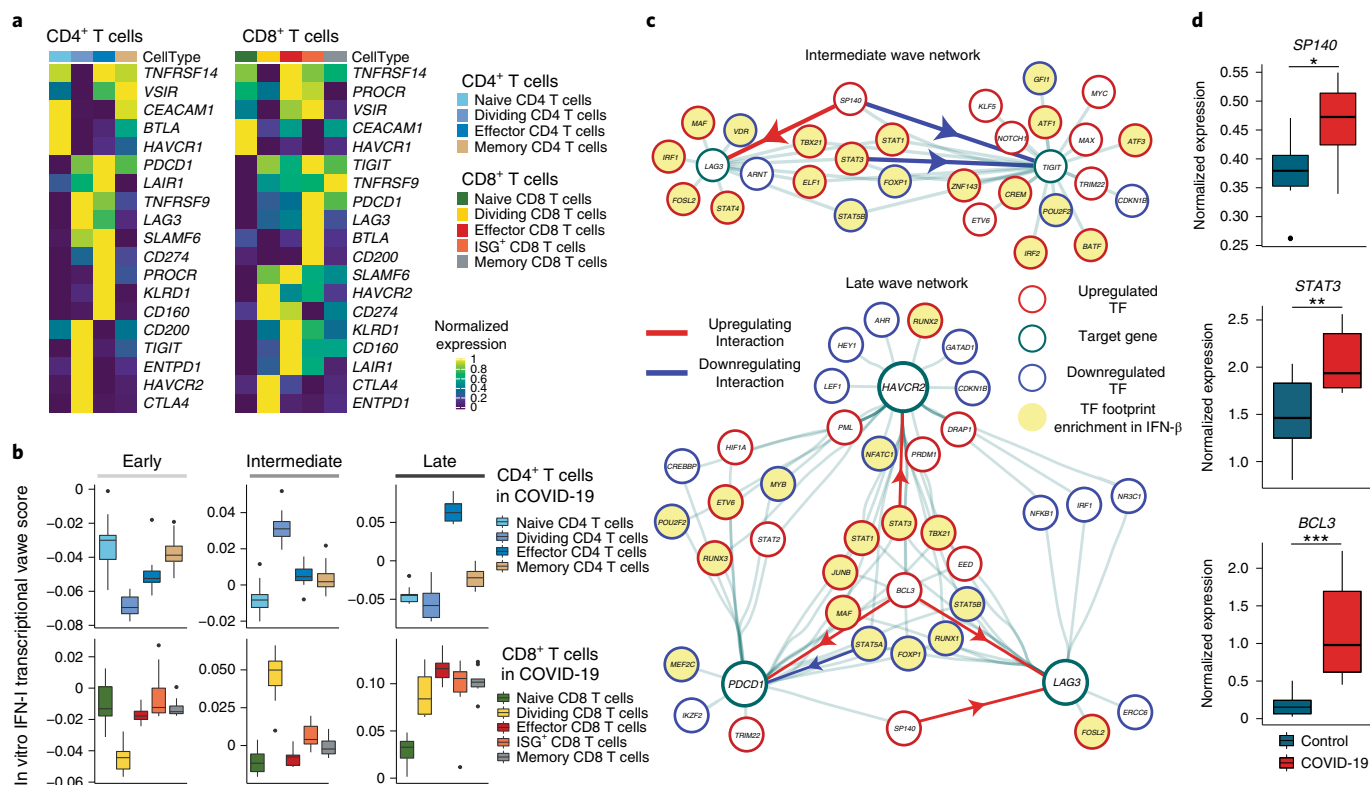


Fig. 6 | Integration of IFN-I regulatory network with T cell signature in COVID-19. **a**, Heatmap showing coinhibitory receptor expression for subsets of CD4⁺ and CD8⁺ T cells in COVID-19. **b**, Scores of computed three transcriptional waves (early, intermediate and late) for the subsets of CD4⁺ and CD8⁺ T cells in COVID-19 patients. Scores were calculated based on upregulated DEGs of CD4⁺ and CD8⁺ T cells for each transcriptional wave. **c**, Regulatory relationship between regulators in intermediate phase network for *LAG3* and *TIGIT* (top) and late phase network for *LAG3*, *HAVCR2* and *PDCD1* (bottom) are shown. Positive regulation (TF to target) is highlighted in red and negative regulation in blue. TF footprints enriched in IFN- β condition were highlighted in yellow. **d**, Boxplots showing expression of key regulators between control and COVID-19 for CD4⁺ T cells. Average expression per subject for each gene is shown. * $P < 0.05$, ** $P < 0.01$, *** $P < 0.001$, using a two-sided Kruskal-Wallis test.

targets for manipulation of specific downstream functional molecules such as coinhibitory receptors in T cells. One of the limitations is that, although our regulatory network takes into account all DEGs by IFN- β treatment, which were further ranked as the key regulatory factors for the enrichment score under treatment with IFN- β , it does not exclude the possibility that they play an important role regulating certain genes or perhaps the same genes under other conditions.

We demonstrate the relevance of our in vitro T cell IFN-I response to humans by integrating scRNA-seq data from COVID-19 patients, in whom a predominant T cell IFN-I response was observed. Intriguingly, the expression pattern of coinhibitory receptors on T cells in vitro are highly replicated in severe COVID-19 cases, and classic ISGs were well correlated with one module of coinhibitory receptors (*LAG3/PDCD1/HAVCR2*), but not with the other modules (*TIGIT/CD160/BTLA/LAIR1*). Although the dynamics of IFN-I on T cells from COVID-19 patients should be considered with higher temporal profiling, we confirmed that the IFN-I response was clearly reduced at a later point; thus, our data based on an earlier collection of blood should reflect the active ISG transcriptomics during human acute viral response. Given that the IFN-I response has been shown to contribute to chronic viral infection and cancer, the new regulators that we identified can be examined in these diseases, because in vitro T cell culture systems only partially model chronic infection or cancer milieu in vivo. Further investigations of factors that characterize acute viral infections are likely to differ from chronic viral infections and will be of interest to explore in the context of long-term human infections not well

modeled by COVID-19. Finally, we have previously shown that TIM-3 is decreased in T cells in patients with multiple sclerosis. As predicted based on our investigations, TIM-3 expression increased in T cells in MS patients after IFN- β treatment⁴³. Further studies in COVID-19 patients who have been treated with IFN- β may provide further insight into the functional relevance of T cell IFN-I response in COVID-19 pathogenesis^{44,45}.

In conclusion, our systems biology approach identified cytokine signals and regulatory mechanisms that drive the expression of coinhibitory receptors in humans, and provided a pathway to comprehensively capture the dynamics of their expression in humans. Our results will advance the understanding of the host immune response to a variety of viral infections and could serve as a resource for mining existing datasets. Uncovering new ISG regulators controlling coinhibitory receptors will create a foundation for further development of new therapeutics for a multitude of different malignant and infectious diseases.

Online content

Any methods, additional references, Nature Research reporting summaries, source data, extended data, supplementary information, acknowledgements, peer review information; details of author contributions and competing interests; and statements of data and code availability are available at <https://doi.org/10.1038/s41590-022-01152-y>.

Received: 21 December 2020; Accepted: 3 February 2022;
Published online: 17 March 2022

References

- Chihara, N. et al. Induction and transcriptional regulation of the co-inhibitory gene module in T cells. *Nature* **558**, 454–459 (2018).
- DeLong, J. H. et al. IL-27 and TCR stimulation promote T cell expression of multiple inhibitory receptors. *Immunohorizons* **3**, 13–25 (2019).
- Curtsinger, J. M., Valenzuela, J. O., Agarwal, P., Lins, D. & Mescher, M. F. Type I IFNs provide a third signal to CD8 T cells to stimulate clonal expansion and differentiation. *J. Immunol.* **174**, 4465–4469 (2005).
- Marrack, P., Kappler, J. & Mitchell, T. Type I interferons keep activated T cells alive. *J. Exp. Med.* **189**, 521–530 (1999).
- Le Bon, A. et al. Direct stimulation of T cells by type I IFN enhances the CD8⁺ T cell response during cross-priming. *J. Immunol.* **176**, 4682–4689 (2006).
- Gonzalez-Navajas, J. M., Lee, J., David, M. & Raz, E. Immunomodulatory functions of type I interferons. *Nat. Rev. Immunol.* **12**, 125–135 (2012).
- Crow, M. K. & Ronnblom, L. Type I interferons in host defence and inflammatory diseases. *Lupus Sci. Med.* **6**, e000336 (2019).
- Musella, M., Manic, G., De Maria, R., Vitale, I. & Sistigu, A. Type-I-interferons in infection and cancer: unanticipated dynamics with therapeutic implications. *Oncimmunology* **6**, e1314424 (2017).
- Welsh, R. M., Bahl, K., Marshall, H. D. & Urban, S. L. Type I interferons and antiviral CD8 T-cell responses. *PLoS Pathog.* **8**, e1002352 (2012).
- Axtell, R. C., Raman, C. & Steinman, L. Type I interferons: beneficial in Th1 and detrimental in Th17 autoimmunity. *Clin. Rev. Allergy Immunol.* **44**, 114–120 (2013).
- Teijaro, J. R. et al. Persistent LCMV infection is controlled by blockade of type I interferon signaling. *Science* **340**, 207–211 (2013).
- Wilson, E. B. et al. Blockade of chronic type I interferon signaling to control persistent LCMV infection. *Science* **340**, 202–207 (2013).
- Baumeister, S. H., Freeman, G. J., Dranoff, G. & Sharpe, A. H. Coinhibitory pathways in immunotherapy for cancer. *Annu. Rev. Immunol.* **34**, 539–573 (2016).
- Anderson, A. C., Joller, N. & Kuchroo, V. K. Lag-3, Tim-3, and TIGIT: co-inhibitory receptors with specialized functions in immune regulation. *Immunity* **44**, 989–1004 (2016).
- Crawford, A. et al. Molecular and transcriptional basis of CD4⁺ T cell dysfunction during chronic infection. *Immunity* **40**, 289–302 (2014).
- Zhen, A. et al. Targeting type I interferon-mediated activation restores immune function in chronic HIV infection. *J. Clin. Invest.* **127**, 260–268 (2017).
- Mestas, J. & Hughes, C. C. Of mice and not men: differences between mouse and human immunology. *J. Immunol.* **172**, 2731–2738 (2004).
- Molle, C. et al. IL-27 synthesis induced by TLR ligation critically depends on IFN regulatory factor 3. *J. Immunol.* **178**, 7607–7615 (2007).
- Petricoin, E. F. 3rd et al. Antiproliferative action of interferon-alpha requires components of T-cell-receptor signalling. *Nature* **390**, 629–632 (1997).
- Marshall, H. D., Urban, S. L. & Welsh, R. M. Virus-induced transient immune suppression and the inhibition of T cell proliferation by type I interferon. *J. Virol.* **85**, 5929–5939 (2011).
- Buenrostro, J. D., Giresi, P. G., Zaba, L. C., Chang, H. Y. & Greenleaf, W. J. Transposition of native chromatin for fast and sensitive epigenomic profiling of open chromatin, DNA-binding proteins and nucleosome position. *Nat. Methods* **10**, 1213–1218 (2013).
- Luoma, A. M. et al. Molecular pathways of colon inflammation induced by cancer immunotherapy. *Cell* **182**, 655–671.e622 (2020).
- Sade-Feldman, M. et al. Defining T cell states associated with response to checkpoint immunotherapy in melanoma. *Cell* **175**, 998–1013.e1020 (2018).
- Oh, D. Y. et al. Intratumoral CD4⁺ T cells mediate anti-tumor cytotoxicity in human bladder cancer. *Cell* **181**, 1612–1625.e1613 (2020).
- Li, H. et al. Dysfunctional CD8 T cells form a proliferative, dynamically regulated compartment within human melanoma. *Cell* **176**, 775–789.e718 (2019).
- Quigley, M. et al. Transcriptional analysis of HIV-specific CD8⁺ T cells shows that PD-1 inhibits T cell function by upregulating BATF. *Nat. Med.* **16**, 1147–1151 (2010).
- Rusinova, I. et al. Interferome v2.0: an updated database of annotated interferon-regulated genes. *Nucleic Acids Res.* **41**, D1040–D1046 (2013).
- Lagette, N. et al. SAMHD1 is the dendritic- and myeloid-cell-specific HIV-1 restriction factor counteracted by Vpx. *Nature* **474**, 654–657 (2011).
- Baldauf, H. M. et al. SAMHD1 restricts HIV-1 infection in resting CD4⁺ T cells. *Nat. Med.* **18**, 1682–1687 (2012).
- Bentsen, M. et al. ATAC-seq footprinting unravels kinetics of transcription factor binding during zygotic genome activation. *Nat. Commun.* **11**, 4267 (2020).
- Gennert, D. G. et al. Dynamic chromatin regulatory landscape of human CAR T cell exhaustion. *Proc. Natl Acad. Sci. USA* **118**, e2104758118 (2021).
- De Vico Fallani, E., Latora, V. & Chavez, M. A topological criterion for filtering information in complex brain networks. *PLoS Comput. Biol.* **13**, e1005305 (2017).
- Hofer, M. J. et al. Mice deficient in STAT1 but not STAT2 or IRF9 develop a lethal CD4⁺ T-cell-mediated disease following infection with lymphocytic choriomeningitis virus. *J. Virol.* **86**, 6932–6946 (2012).
- Grunwell, J. R. et al. TGF-beta1 suppresses the type I IFN response and induces mitochondrial dysfunction in alveolar macrophages. *J. Immunol.* **200**, 2115–2128 (2018).
- Thomas, D. A. & Massague, J. TGF-beta directly targets cytotoxic T cell functions during tumor evasion of immune surveillance. *Cancer Cell* **8**, 369–380 (2005).
- Uterman, A. et al. Single-cell omics reveals dyssynchrony of the innate and adaptive immune system in progressive COVID-19. *Nat. Commun.* **13**, 440 (2022).
- Mostafavi, S. et al. Parsing the interferon transcriptional network and its disease associations. *Cell* **164**, 564–578 (2016).
- Grosso, J. F. et al. LAG-3 regulates CD8⁺ T cell accumulation and effector function in murine self- and tumor-tolerance systems. *J. Clin. Invest.* **117**, 3383–3392 (2007).
- Terawaki, S. et al. IFN-alpha directly promotes programmed cell death-1 transcription and limits the duration of T cell-mediated immunity. *J. Immunol.* **186**, 2772–2779 (2011).
- Ghiboub, M. et al. Modulation of macrophage inflammatory function through selective inhibition of the epigenetic reader protein SP140. Preprint at *bioRxiv*, <https://doi.org/2020.2008.2010.239475> (2020).
- Gil, M. P. et al. Biologic consequences of Stat1-independent IFN signaling. *Proc. Natl Acad. Sci. USA* **98**, 6680–6685 (2001).
- Wang, W., Xu, L., Su, J., Peppelenbosch, M. P. & Pan, Q. Transcriptional regulation of antiviral interferon-stimulated genes. *Trends Microbiol.* **25**, 573–584 (2017).
- Yang, L., Anderson, D. E., Kuchroo, J. & Hafler, D. A. Lack of TIM-3 immunoregulation in multiple sclerosis. *J. Immunol.* **180**, 4409–4414 (2008).
- Monk, P. D. et al. Safety and efficacy of inhaled nebulised interferon beta-1a (SNG001) for treatment of SARS-CoV-2 infection: a randomised, double-blind, placebo-controlled, phase 2 trial. *Lancet Respir. Med.* **9**, 196–206 (2021).
- Bosi, E. et al. Interferon beta-1a (IFNbeta-1a) in COVID-19 patients (INTERCOP): study protocol for a randomized controlled trial. *Trials* **21**, 939 (2020).

Publisher's note Springer Nature remains neutral with regard to jurisdictional claims in published maps and institutional affiliations.

© The Author(s), under exclusive licence to Springer Nature America, Inc. 2022

Methods

Study subjects. Peripheral blood was drawn from healthy controls who were recruited as part of an institutional review board-approved study at Yale University, and written consent was obtained. All experiments conformed to the principles set out in the World Medical Association's Declaration of Helsinki and the Department of Health and Human Services Belmont Report.

Human T cell isolation and culture. Peripheral blood mononuclear cells (PBMCs) were prepared from whole blood by Ficoll gradient centrifugation (Lymphoprep, STEMCELL Technologies) and used directly for total T cell enrichment by negative magnetic selection using Easysep magnetic separation kits (STEMCELL Technologies). Cell suspension was stained with anti-CD4 (RPA-T4), anti-CD8 (catalog no. RPA-T8), anti-CD25 (clone 2A3), anti-CD45RO (catalog no. UCHL1), anti-CD45RA (catalog no. HI100) and anti-CD127 (catalog no. hIL-7R-M21) (all from BD Biosciences) for 30 min at 4 °C. Naive CD4⁺ T cells (CD4⁺/CD25^{neg}/CD127⁺/CD45RO^{neg}/CD45RA⁺) and naive CD8⁺ T cells (CD8⁺/CD25^{neg}/CD127⁺/CD45RO^{neg}/CD45RA⁺) were sorted on a FACSAria (BD Biosciences). Sorted cells were plated in 96-well, round-bottomed plates (Corning) and cultured in RPMI 1640 medium supplemented with 5% human serum, 2 nM L-glutamine, 5 mM Hepes, 100 U ml⁻¹ of penicillin, 100 µg ml⁻¹ of streptomycin, 0.5 mM sodium pyruvate, 0.05 mM nonessential amino acids and 5% human AB serum (Gemini Bio-Products). Cells were seeded (30,000–50,000 per well) into wells pre-coated with anti-human CD3 (2 µg ml⁻¹, clone UCHT1, BD Biosciences) along with soluble anti-human CD28 (1 µg ml⁻¹, clone 28.2, BD Biosciences) in the presence or absence of human IFN-β (500 U ml⁻¹; Pestka Biomedical Laboratories) or IL-27 (100 ng ml⁻¹; BioLegend) without adding IL-2. To avoid interindividual batch effects, T cells used for RNA-seq and ATAC-seq were isolated from one individual (37-year-old, healthy man with no evidence of viral infection, cancer or autoimmune diseases at the time of sample collection).

Lentiviral and Vpx-VLP production. Lentiviral plasmids encoding shRNA for gene knockdown or open reading frame (ORF) of STAT5A for overexpression were obtained from Sigma-Aldrich (MISSION shRNA, Sigma-Aldrich) and Horizon Discovery Biosciences (Precision LentiORF), respectively. Scrambled shRNA (Sigma-Aldrich; for perturbation experiment) or GFP control vectors (Origene, for protein validation experiment; Horizon Discovery Bioscience, for overexpression experiment) are used as the controls for lentiviral transduction. Each plasmid was transformed into One Shot Stbl3 chemically competent cells (Invitrogen) and purified by ZymoPURE plasmid Maxiprep kit (Zymo Research). Lentiviral pseudoparticles were obtained after plasmid transfection of 293T cells using Lipofectamine 2000 (Invitrogen) or TurboFectin 8.0 Transfection Reagent (Origene). To prepare Vpx-VLPs, 293T cells were cotransfected by Lipofectamine 2000 or TurboFectin 8.0 Transfection Reagent with the 5 µg of pMDL-X, 2.5 µg of pcRSV-Rev, 3.5 µg of X4-tropic HIV Env and 1 µg of pcVpx/myc, as described previously with some modifications^{37,38}. The medium was replaced after 6–12 h with fresh medium with 1× viral boost (Alstem). The lentivirus- or Vpx-VLP-containing medium was harvested 72 h after transfection and concentrated 80× using Lenti-X concentrator (Takara Clontech) or Lenti Concentrator (Origene). Lentiviral particles were then resuspended in RPMI 1640 medium without serum and stored at -80 °C before use. Virus titer was determined by using Jurkat T cells and Lenti-X GoStix Plus (Takara Clontech).

Lentiviral transduction with Vpx-VLPs. Two-step Vpx-VLP and lentiviral transduction were performed as described previously with some modifications³⁶. Vpx are pseudotyped with X4-tropic HIV Env to promote efficient entry of Vpx-VLPs into quiescent human T cells³⁷. FACS-sorted naive CD4⁺ T cells were plated at 50,000 cells per well in round-bottomed, 96-well plates and chilled on ice for 15 min. Then 25–50 µl of Vpx-VLPs was added to each well and mixed with cold cells for an additional 15 min, then spinfected with high-speed centrifugation (1,200g) for 2 h at 4 °C. Immediately after centrifugation, cells are cultured overnight at 37 °C. Vpx-transduced cells are spinoculated again with lentiviral particles containing shRNAs or ORF with high-speed centrifugation (1,000g) for 1.5 h at room temperature. After 24 h of incubation, the second transduction of lentiviral particles with shRNAs or ORF was performed as well as the first-time spinoculation. After a second lentiviral transduction, cells were washed and plated into 96-well, round-bottomed plates pre-coated with anti-human CD3 (2 µg ml⁻¹) and soluble anti-human CD28 (1 µg ml⁻¹), in the presence or absence of human IFN-β (500 U ml⁻¹). Cells were collected at days 4–6 after anti-CD3/CD28 stimulation and GFP-positive cells were sorted by FACSAria or analyzed by Fortessa.

Real-time qPCR. Total RNA was extracted using RNeasy Micro Kit (QIAGEN) or ZR-96 Quick-RNA kit (Zymo Research), according to the manufacturer's instructions. RNA was treated with DNase and reverse transcribed using TaqMan Reverse Transcription Reagents (Applied Biosystems) or SuperScript IV VILO Master Mix (Invitrogen). Complementary DNAs were amplified with Taqman probes (Supplementary Table 2) and TaqMan Fast Advanced Master Mix on a StepOne Real-Time PCR System (Applied Biosystems) according to

the manufacturer's instructions. Relative mRNA expression was evaluated after normalization with *B2M* expression.

Flow cytometry analysis. Cells were stained with a LIVE/DEAD Fixable Near-IR Dead Cell Stain kit (Invitrogen) and surface antibodies for 30 min at 4 °C. For intracellular cytokine staining, cells were treated with 50 nM phorbol-12-myristate-13-acetate (MilliporeSigma) and 250 nM ionomycin (MilliporeSigma) for 4 h in the presence of Brefeldin A (BD Biosciences) before harvesting. Cells were washed and fixed with BD Cytotfix Fixation Buffer (BD Biosciences) for 10 min at room temperature, then washed with phosphate-buffered saline. Intracellular cytokines were stained in permeabilization buffer (eBioscience) for 30 min at 4 °C. Antibody details are provided in Supplementary Table 3. Cells were acquired on a BD Fortessa flow cytometer with FACSDiva (BD Pharmingen) and data were analyzed with FlowJo software v.10 (Threestar).

RNA-seq library preparation and data analysis. Then, 10,000 cells per condition were subjected to RNA-seq. The cDNAs were generated from isolated RNAs using SMART-Seq v.4 Ultra Low Input RNA Kit for sequencing (Takara/Clontech). Barcoded libraries were generated by the Nextera XT DNA Library Preparation kit (Illumina) and sequenced with a 2×100 bp paired-end protocol on the HiSeq 4000 Sequencing System (Illumina).

After sequencing, adapter sequences and poor-quality bases (quality score <3) were trimmed with Trimmomatic. The remaining bases were trimmed if their average quality score in a 4-bp sliding window fell <5. FastQC was used to obtain quality control metrics before and after trimming. Remaining reads were aligned to the GRCh38 human genome with STAR 2.5.2 (ref. 46). We used Picard to remove optical duplicates and to compile alignment summary statistics and RNA-seq summary statistics. After alignment, reads were quantified to gene level with RSEM (RNA-seq by expectation-maximization)⁴⁷ using the Ensembl annotation. Normalized fragments per kilobase million (FPKM) expression values of the three replicates were used for the analysis below.

Identification of three transcriptional waves. The correlation matrix is created by Pearson correlating⁴⁸ the IFN-β expression profile of each timepoint with all the other timepoints, creating a symmetrical matrix of Pearson's correlation coefficients.

Differential expression calculation. The differential expression⁴⁹ for each timepoint was calculated using the DESeq2 (ref. 50) R package. Three separate testing methods were used for calculating DEGs: Wald⁵¹, likelihood ratio test⁵² and time course⁵³. For each of the three methods, genes with a false discovery rate (FDR)-adjusted *P* value <0.05 were regarded as differentially expressed. More specifically, for CD4⁺ T cells, if TFs appeared in two of the three calculating methods (agree by two), they were regarded as differentially expressed. For CD8⁺ T cells, if TFs appeared in any of the methods above, they were regarded as differentially expressed.

Selection of regulators for perturbation. The list of TFs for perturbation was selected based on the following criteria: (1) overlapped DETFs across the timepoints between CD4⁺ and CD8⁺ T cells based on the above-mentioned method; intersection of DETFs in our in vitro data were chosen; (2) DETFs in human TILs^{22–25} that were significantly correlated with exhausted T cell cluster (defined by the upregulation of LAG-3/PD-1/TIM-3); 'human TIL score', defined as the number of times a gene was shared between the four different human cancer TIL datasets; (3) HIV-specific T cell signature upregulated in progressive patients compared with stable patients²⁶; and (4) TFs that were induced by IL-27 and categorized as IL-27-driven coinhibitory receptor modules¹; 'human ISG score' is defined as the number of times it was shared across the three different categories (T cells, PBMCs and all immune cells) of human ISGs identified by the Interferome database. All perturbed TFs were confirmed as IFN-I-induced genes and showed 'human ISG score' >1.

DEGs heatmap. Expression data of all timepoints under IFN-β treatment expression were divided by the control expression data, creating fold-change ratio data of treatment over control. For visualization purposes, the fold-change data in Fig. 2a were then shown for the DEGs only, logged to a base of 10 and scaled per row. The results were clustered hierarchically. In Fig. 2c specific genes of interest were picked, such as ISGs, coinhibitory receptors, T cell-related genes and TFs.

Heatmap of perturbed TFs. Twenty-one TFs were perturbed using lentiviral shRNA, together with a scrambled shRNA (SCR) as control. ISGs (IFN score B³⁴) and coinhibitory receptors were selected to visualize the expression differences in the two modules, in Extended Data Fig. 5b,c. The effect of TF perturbation on IFN-β response for each gene of interest (GOI) was calculated as follows: for each shRNA perturbation, the effect of IFN-β treatment over control condition was calculated for GOIs. This fold-change value was then logged to a base of 2. To normalize the effect of the shRNA protocol, we further normalized the data by the SCR, in an identical manner to the shRNA perturbation described above. Finally, the log₂(transformed shRNA values) were subtracted by the log₂(transformed SCR values) as shown in the equation below:

$$\log_2 \left(\frac{\text{GOI expression in perturbed TF+IFN}\beta \text{ treatment}}{\text{GOI expression}} \right) \text{ in perturbed TF} \\ - \log_2 \left(\frac{\text{GOI expression in SCR+IFN}\beta \text{ treatment}}{\text{GOI expression in SCR}} \right)$$

For the heatmap visualization, the normalized values calculated by the equation above were clustered hierarchically.

Differential expression analysis for each TF perturbation was conducted as follows: perturbed TF + IFN- β treatment expression versus perturbed TF untreated expression. DEGs in this analysis that were regarded as significant (FDR-adjusted $P < 0.05$) were marked with a white plus sign on their tile.

PCA and PCA biplot analysis. The PCA was applied to the DEGs (defined above) as variables and perturbed genes as observations. The data were normalized by the SCR control, in the same manner as the heatmap of perturbed TFs. Although *PDCD1* was not defined as a DEG across the time course, it was differentially expressed at later timepoints in mRNA-seq and qPCR, so we manually added it to Fig. 5f. Genes of IFN score B³¹ (Supplementary Table 1) were represented as ISGs in Fig. 3e. The PCA and biplot analysis were calculated and visualized using the R package FactoMineR⁵³.

Regulatory networks. After the differentially expressed analysis in each transcriptional wave, the DEGs were defined as TFs and their targets (from \rightarrow to). The targets of all DETFs were determined using chromatin immunoprecipitation with sequencing (ChIP-seq) data from the database GTRD⁵⁶. TFs and target genes defined as differentially expressed were added to the network as nodes (circles) and edges (lines) were added between them. The network plots were created using the Cytoscape⁵⁷ software.

Top regulatory TFs heatmaps. We ranked the DETFs of each transcriptional time wave to identify the dominant regulators in each stage of the differentiation process using two methods. HG values were the values in the heatmap that are the $\log(P)$ value of the HG enrichment test $-\log_{10}(P \text{ value})$. The HG calculation was conducted using the python SciPy package⁵⁸. The second method used network Cent, which is a parameter that is given to each node, based on the shortest path from the node to the other nodes in the network. It represents how central and connected a node is to the rest of the network⁵⁹. The Cent calculation was conducted using the python NetworkX⁶⁰ package. The rank column is an average of both HG and Cent values, after scaling to the range of 0–1.

Integration of perturbation data to regulatory networks. After the generation of the regulatory network mentioned above, we further refined the network by integrating the TF perturbation data. Genes that were significantly affected by a TF perturbation were added as ‘validated’ edges between the perturbed TF and the target gene. If a gene was upregulated by a TF perturbation, the interaction between them was registered as downregulation. If a gene was downregulated by a TF perturbation, the interaction between them was registered as upregulation.

Reduced TF networks. For visualization purposes we used a network reduction algorithm. The algorithm presents all the TFs in the network (nodes) but reduces some of the connections between them (edges). The reduced TF networks were calculated using the NetworkToolbox⁶¹ package in Rstudio. The method of the reduction calculation was ECOplusMaST⁶², which applies the efficiency cost optimization, neural network-filtering method combined with the Maximum Spanning Tree-filtering⁶² method.

The barplots depicted at the bottom represent the mean level of the degree⁶³ value for either up- or downregulated TFs, in the complete networks (not reduced ones). The degree of a node is the number of connections that it has to other nodes. An independent two-way Student's *t*-test was conducted between the degree values of the up and down TFs for each time wave. The *P* value of each test is presented in the caption of each barplot.

Bridging TFs network. DETFs and their target genes from the three transcriptional waves were combined to create a comprehensive network emphasizing the dynamics between transcriptional waves. In this network TFs and their target genes were annotated by the transcriptional wave in which they appear as differentially expressed. TFs that participate in more than one transcriptional wave are regarded as bridging TFs.

ATAC-seq library preparation and data analysis. Cells were split into RNA-seq (10,000 cells) and ATAC-seq (15,000 cells) at the time of collection. Cells for ATAC-seq were cryopreserved using Recovery Cell Culture Freezing Medium (Gibco) with a concentration of 15,000 cells per 100 μ l. Cryopreserved cells were thawed and immediately proceeded to Tn5 digestion (50 μ l of transposase mixture: 25 μ l of 2 \times TD buffer, 2.5 μ l of TDE1 (both from Illumina), 0.5 μ l of 1% digitonin (Promega) and 22 μ l of nuclease-free water)⁶⁴. Transposition reactions were incubated at 37 $^{\circ}$ C for 30 min in a thermal shaker with agitation at 300 r.p.m. Transposed DNA was purified using a Zymo DNA Clean and Concentrator-5 Kit (Zymo Research) and purified DNA was eluted in 10 μ l of elution buffer.

Transposed fragments were amplified and purified as described previously⁶⁴ with modified primers⁶⁵. Libraries were quantified using qPCR (KAPA Library Quantification Kit) before sequencing. All ATAC libraries were sequenced using a 2 \times 150-bp paired-end protocol on the Nova-seq Sequencing System (Illumina).

ATAC-seq alignment, feature calling and quantification. We trimmed adapter sequences before aligning reads to the GRCh38 human genome assembly with Bowtie 2. We used FastQC (<http://www.bioinformatics.babraham.ac.uk/projects/fastqc>) to obtain sequence quality control metrics both before and after read trimming. We obtained alignment summary metrics with Picard tools (<http://broadinstitute.github.io/picard>). We retained reads that mapped uniquely to the primary assembly with mapping quality ≥ 30 and removed optical duplicates. We shifted cut sites by +4 bp and -5 bp on positive and negative strands, respectively.

We used MACS2 (ref. ⁶⁶) to call ATAC-seq peaks within individual samples using a $q < 0.2$ threshold. For each library, we use ataq⁶⁷ to calculate transcription start site enrichment and the fraction of reads in peaks. We excluded peaks within ENCODE blacklist regions.

We used Markov clustering⁶⁸ to identify a preliminary set of consensus features across libraries. Edges were weighted by the proportion of overlapping bases between each pair of peaks. Peaks that did not overlap with at least one peak from another library were excluded from further analysis. After clustering, we defined preliminary clusters to be the maximal (union) coordinates of all constituent peaks.

We used a two-state hidden Markov model to identify the central, maximally replicated portion of each preliminary feature. Consensus features were defined as the maximal extent of all ‘open’ segments within each cluster.

We used featureCounts⁶⁹ to quantify the number of reads within each peak for each library. Outliers were identified through PCA.

ATAC-seq sample PCA. The PCA was conducted on ATAC-seq peaks from 19 CD4⁺ T cell samples and 21 CD8⁺ T cell samples. Two samples were removed from the CD4⁺ samples due to large variability relative to the other replicates.

Differential chromatin accessibility. Differentially accessible ATAC peaks were calculated using DESeq2 R package. Peaks with FDR-adjusted $P < 0.05$ and fold-change of ± 1 are regarded as differentially accessible peaks.

TF footprint analysis. We used TOBIAS³⁰ to identify TF footprints within accessible chromatin features. We pooled libraries by cell type (CD4⁺ and CD8⁺ T cells) and treatment status (control and IFN- β) at 2-, 8- and 72-h timepoints. Within each pool, we corrected for Tn5 cut site bias and calculated footprint scores with TOBIAS. We used TOBIAS to identify TF motifs differentially footprinted at each timepoint.

Reanalysis of COVID-19 scRNA-seq data. A PBMC scRNA-seq dataset of 10 COVID-19 patients and 13 matched controls, which had been previously performed and reported by us³⁶, was reanalyzed. We have described the full cohort and detailed methods³⁶. From eight of the ten COVID-19 samples, PBMCs from two different timepoints had been analyzed. Four of the COVID-19 patients had been classified as progressive and the other six as stable. Briefly, single-cell barcoding of PBMCs and library construction had been performed using the 10 \times Chromium NextGEM 5prime kit. Libraries had been sequenced on an Illumina Nova-seq 6000 platform. Raw reads had been demultiplexed and processed using Cell Ranger (v.3.1) mapping to the GRCh38 (Ensembl 93) reference genome. The resulting gene–cell matrices had been analyzed using the package Seurat⁴³ in the software R, including integration of data, clustering, multiplet identification and cell-type annotation. The final annotated R object was used and reanalyzed in Seurat with default settings—unless otherwise specified—as follows.

The three cell populations ‘Dividing T & NK’, ‘Effector T’ and ‘Memory CD4 & MAIT’ were each subsetted and reclustered to obtain a finer cell-type granularity because they included a mix of CD4, CD8, MAIT and $\gamma\delta$ T cells. Per subset, the top 500 variable genes were determined by the ‘FindVariableFeatures’ function using the ‘vst’ method. Data were scaled using the ‘ScaleData’ function regressing out the total number of unique molecular identifiers (UMIs) and the percentage of UMIs arising from the mitochondrial genome. After PCA, the first ten PCs were utilized to detect the nearest neighbors using the ‘FindNeighbors’ function and clustered by Seurat’s Louvain algorithm implementation ‘FindClusters’ using a resolution of 0.2 for ‘Dividing T & NK’, 0.3 for ‘Effector T’ and 0.1 for ‘Memory CD4 & MAIT’ subsets. Cluster-specific gene expression profiles were established using the ‘FindAllMarkers’ per cluster and per subset to annotate the clusters. New cell-type annotations were then transferred back to the full dataset.

A new Uniform Approximation and Projection (UMAP) embedding was created by integrating the datasets on a subject level as follows: a subset containing all T cells was generated, which was then split by subject. For each subject, the top 2,000 variable genes were selected, then integration anchors determined by ‘FindIntegrationAnchors’ (with $k.filter = 150$). These anchors were used to integrate the data using the ‘IntegrateData’ function with the top 30 dimensions. The integrated data were scaled, subjected to a PCA and the top 13 PCs used as input for the ‘RunUMAP’ function on 75 nearest neighbors.

Module scores were calculated using the 'AddModuleScore' function using (1) all genes within the gene ontology list 'RESPONSE TO TYPE I INTERFERON' (GO:0034340)⁶⁴ and (2) all genes significantly associated with either of the three waves in our in vitro perturbation experiments (Supplementary Table 1). Differential gene expression was established using Seurat's implementation of Wilcoxon's rank-sum test within the 'FindMarkers' function with Bonferroni's correction for multiple testing.

Statistical analysis. Detailed information about statistical analysis, including tests and values used, is provided in the figure legends. *P* values ≤ 0.05 were considered to be significant.

Reporting Summary. Further information on research design is available in the Nature Research Reporting Summary linked to this article.

Data availability

The sequence data generated in the present study are available under accession no. GSE195543. scRNA-seq data in the present study are available at accession no. GSE155223. Source data are provided with this paper.

References

- Dobin, A. et al. STAR: ultrafast universal RNA-seq aligner. *Bioinformatics* **29**, 15–21 (2013).
- Li, B. & Dewey, C. N. RSEM: accurate transcript quantification from RNA-Seq data with or without a reference genome. *BMC Bioinform.* **12**, 323 (2011).
- Ly, A., Marsman, M. & Wagenmakers, E. J. Analytic posteriors for Pearson's correlation coefficient. *Stat. Neerl.* **72**, 4–13 (2018).
- Bojnordi, M. N. et al. Differentiation of spermatogonia stem cells into functional mature neurons characterized with differential gene expression. *Mol. Neurobiol.* **54**, 5676–5682 (2017).
- Love, M. I., Huber, W. & Anders, S. Moderated estimation of fold change and dispersion for RNA-seq data with DESeq2. *Genome Biol.* **15**, 550 (2014).
- Chen, Y. M., Weng, Y. T., Dong, X. & Tsong, Y. Wald tests for variance-adjusted equivalence assessment with normal endpoints. *J. Biopharm. Stat.* **27**, 308–316 (2017).
- Rubinstein, M. L., Kraft, C. S. & Parrott, J. S. Determining qualitative effect size ratings using a likelihood ratio scatter matrix in diagnostic test accuracy systematic reviews. *Diagnosis* **5**, 205–214 (2018).
- Leong, H. S. et al. A global non-coding RNA system modulates fission yeast protein levels in response to stress. *Nat. Commun.* **5**, 3947 (2014).
- El-Sherbiny, Y. M. et al. A novel two-score system for interferon status segregates autoimmune diseases and correlates with clinical features. *Sci. Rep.* **8**, 5793 (2018).
- Lê, S., Josse, J. & Husson, F. FactoMineR: an R package for multivariate analysis. *J. Statist. Software* **25**, 1–18 (2008).
- Yevshin, I., Sharipov, R., Kolmykov, S., Kondrakhin, Y. & Kolpakov, F. GTRD: a database on gene transcription regulation-2019 update. *Nucleic Acids Res.* **47**, D100–D105 (2019).
- Shannon, P. et al. Cytoscape: a software environment for integrated models of biomolecular interaction networks. *Genome Res.* **13**, 2498–2504 (2003).
- Virtanen, P. et al. SciPy 1.0: fundamental algorithms for scientific computing in Python. *Nat. Methods* **17**, 261–272 (2020).
- Piraveenan, M., Prokopenko, M. & Hossain, L. Percolation centrality: quantifying graph-theoretic impact of nodes during percolation in networks. *PLoS ONE* **8**, e53095 (2013).
- Hagberg, A., Swart, P. & Chult, D. *Exploring Network Structure, Dynamics, and Function Using NetworkX*. United States. <https://www.osti.gov/servlets/purl/960616> (2008).
- Christensen, A. P. NetworkToolbox: methods and measures for brain, cognitive, and psychometric network analysis in R. *R J.* **10**, 422–439 (2018).
- Szalkai, B., Varga, B. & Grolmusz, V. Mapping correlations of psychological and structural connectome properties of the dataset of the human connectome project with the maximum spanning tree method. *Brain Imaging Behav.* **13**, 1185–1192 (2019).
- Rubinov, M. & Sporns, O. Complex network measures of brain connectivity: uses and interpretations. *Neuroimage* **52**, 1059–1069 (2010).
- Corces, M. R. et al. An improved ATAC-seq protocol reduces background and enables interrogation of frozen tissues. *Nat. Methods* **14**, 959–962 (2017).
- Buenrostro, J. D. et al. Single-cell chromatin accessibility reveals principles of regulatory variation. *Nature* **523**, 486–490 (2015).
- Zhang, Y. et al. Model-based analysis of ChIP-Seq (MACS). *Genome Biol.* **9**, R137 (2008).
- Orchard, P., Kyono, Y., Hensley, J., Kitzman, J. O. & Parker, S. C. J. Quantification, dynamic visualization, and validation of bias in ATAC-Seq data with ataqv. *Cell Syst.* **10**, 298–306.e294 (2020).
- Enright, A. J., Van Dongen, S. & Ouzounis, C. A. An efficient algorithm for large-scale detection of protein families. *Nucleic Acids Res.* **30**, 1575–1584 (2002).
- Liao, Y., Smyth, G. K. & Shi, W. featureCounts: an efficient general purpose program for assigning sequence reads to genomic features. *Bioinformatics* **30**, 923–930 (2014).

Acknowledgements

We thank L. Devine and C. Wang for assistance with FACS-based cell sorting, G. Wang, M. Machado and C. Castaldi at Yale Center for Genome Analysis for support with 10x Genomics library and ATAC-seq library preparation and sequencing, P. Coish for his diligent proofreading of this paper, K. Raddassi and L. Zhang for processing scRNA-seq samples, L. Geng and M. Zhang for preparation of the bulk RNA-seq libraries and sequencing, M. Taura for assistance developing Vpx-VLP-based lentiviral transduction and N. Chihara and H. Asashima for useful discussions and input on the manuscript. This work was supported by grants to T.S.S. from Race to Erase MS, to M.R.L. from the National MS Society and the Consortium of MS Centers (Career Transition Award), to D.A.H. from the National Institutes of Health (NIH) (grant nos. U19 AI089992, R25 NS079193, P01 AI073748, P01 AI039671 and P50 CA121974), the National Multiple Sclerosis Society (grant nos. CA 1061-A-18 and RG-1802-30153), the Nancy Taylor Foundation for Chronic Diseases and Erase MS, to V.K.K. from NIH (grant nos. R01 NS045937, R01 NS030843, R01 AI144166, P01 AI073748, P01 AI039671 and P01 AI056299) and the Klarman Cell Observatory, to N.K. from NIH (grant nos. R01HL127349, R01HL141852 and U01HL145567), to A.M. from The Alon fellowship for outstanding young scientists, Israel Council for Higher Education, the Israel Science Foundation (1700/21), the Israel Cancer Association (01028753) and the Israel Cancer Research Fund Research Career Development Awards, and to J.C.S. from DoD (grant no. W81XWH-19-1-0131). The RNA-seq service was conducted at Yale Center for Genome Analysis and Yale Stem Cell Center Genomics Core facility, the latter supported by the Connecticut Regenerative Medicine Research Fund and the Li Ka Shing Foundation.

Author contributions

T.S.S., A.M., V.K.K. and D.A.H. conceptualized the study. T.S.S. performed in vitro experiments with the help of H.A.S., M.C. and P.P.A. T.S.S. prepared sequencing libraries. M.R.L. processed bulk RNA-seq and ATAC-seq data alignment. S.D. and A.M. performed computational analysis to construct a gene-regulatory network with input from T.S.S. J.C.S. performed scRNA-seq analysis on COVID-19 data with the help of T.S.S., A.U. and N.K. T.S.S., S.D., J.C.S., A.M. and D.A.H. wrote the manuscript with input from all authors. T.S.S., A.M., V.K.K. and D.A.H. supervised the overall study.

Competing interests

D.A.H. has received research funding from Bristol-Myers Squibb, Sanofi and Genentech. He has been a consultant for Bristol-Myers Squibb, Compass Therapeutics, EMD Serono, Genentech and Sanofi Genzyme over the last 3 years. Further information about funding is available at <https://openpaymentsdata.cms.gov/physician/166753>. V.K.K. has an ownership interest and is a member of the SAB for Tizona Therapeutics. V.K.K. is also a cofounder and has an ownership interest, and is a member of the SAB in Celsius Therapeutics and Bicara Therapeutics. V.K.K.'s interests were reviewed and managed by the Brigham and Women's Hospital and Partners Healthcare in accordance with their conflict-of-interest policies. N.K. served as a consultant to Biogen Idec, Boehringer Ingelheim, Third Rock, Pliant, Samumed, NuMedii, Theravance, LifeMax, Three Lake Partners, Optikira and Astra Zeneca over the last 3 years, and reports Equity in Pliant and a grant from Veracyte and nonfinancial support from MiRagen and Astra Zeneca. He has intellectual property (IP) on new biomarkers and therapeutics in idiopathic pulmonary fibrosis (IPF) licensed to Biotech. The remaining authors declare no competing interests.

Additional information

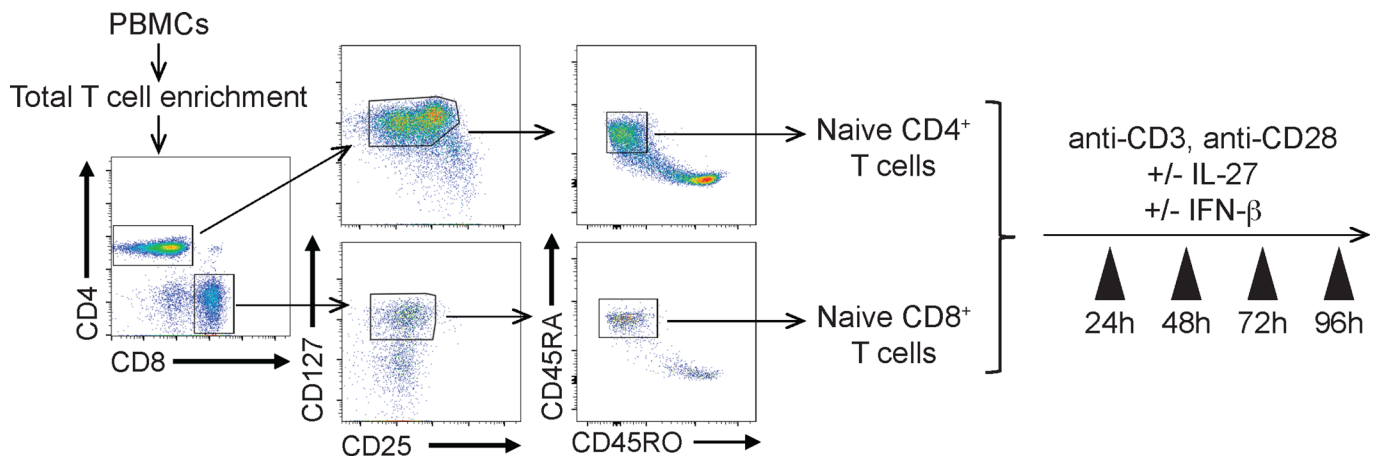
Extended data are available for this paper at <https://doi.org/10.1038/s41590-022-01152-y>.

Supplementary information The online version contains supplementary material available at <https://doi.org/10.1038/s41590-022-01152-y>.

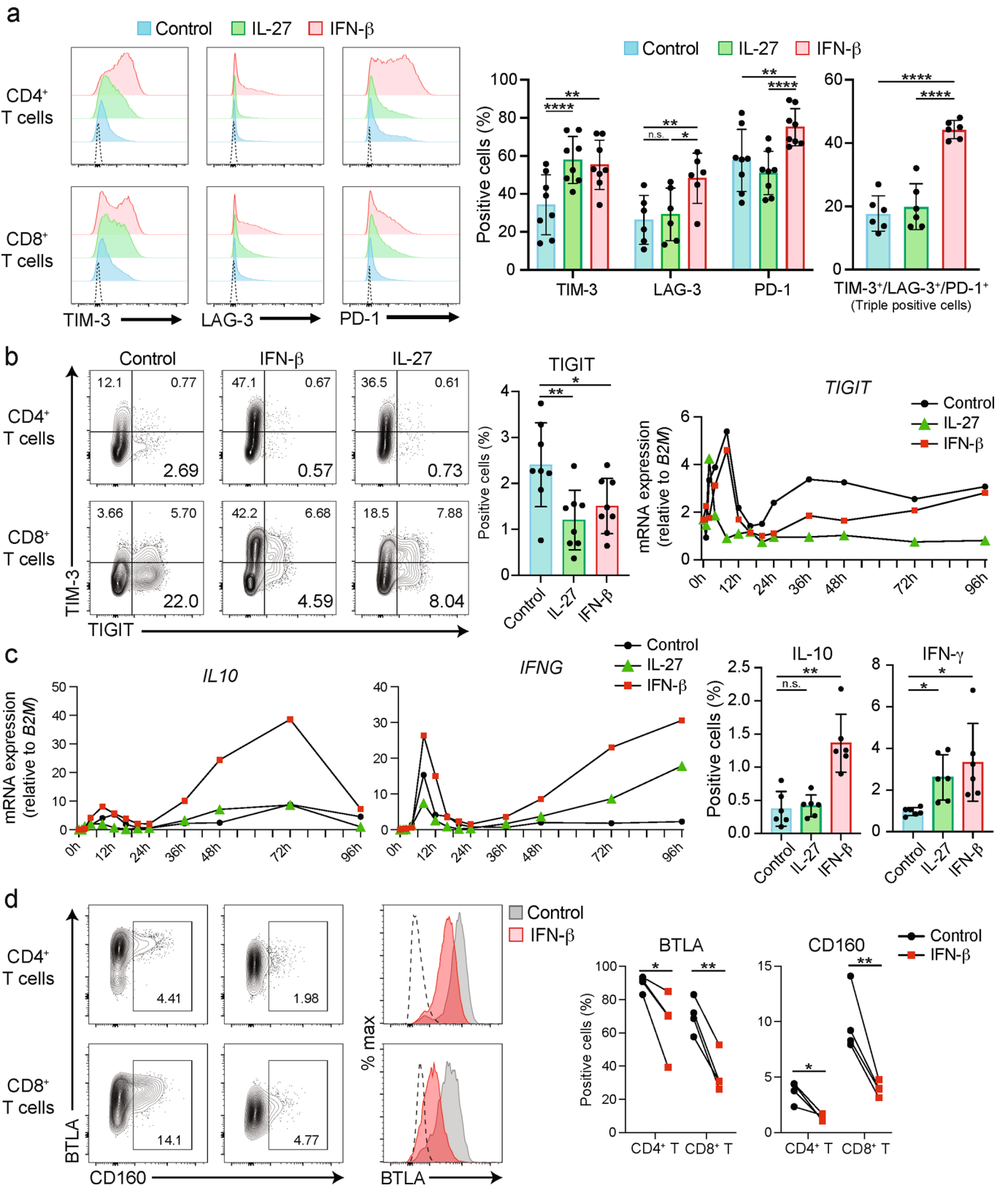
Correspondence and requests for materials should be addressed to Tomokazu S. Sumida or Asaf Madi.

Peer review information *Nature Immunology* thanks the anonymous reviewers for their contribution to the peer review of this work. Zoltan Fehervari was the primary editor on this article and managed its editorial process and peer review in collaboration with the rest of the editorial team. Peer reviewer reports are available.

Reprints and permissions information is available at www.nature.com/reprints.

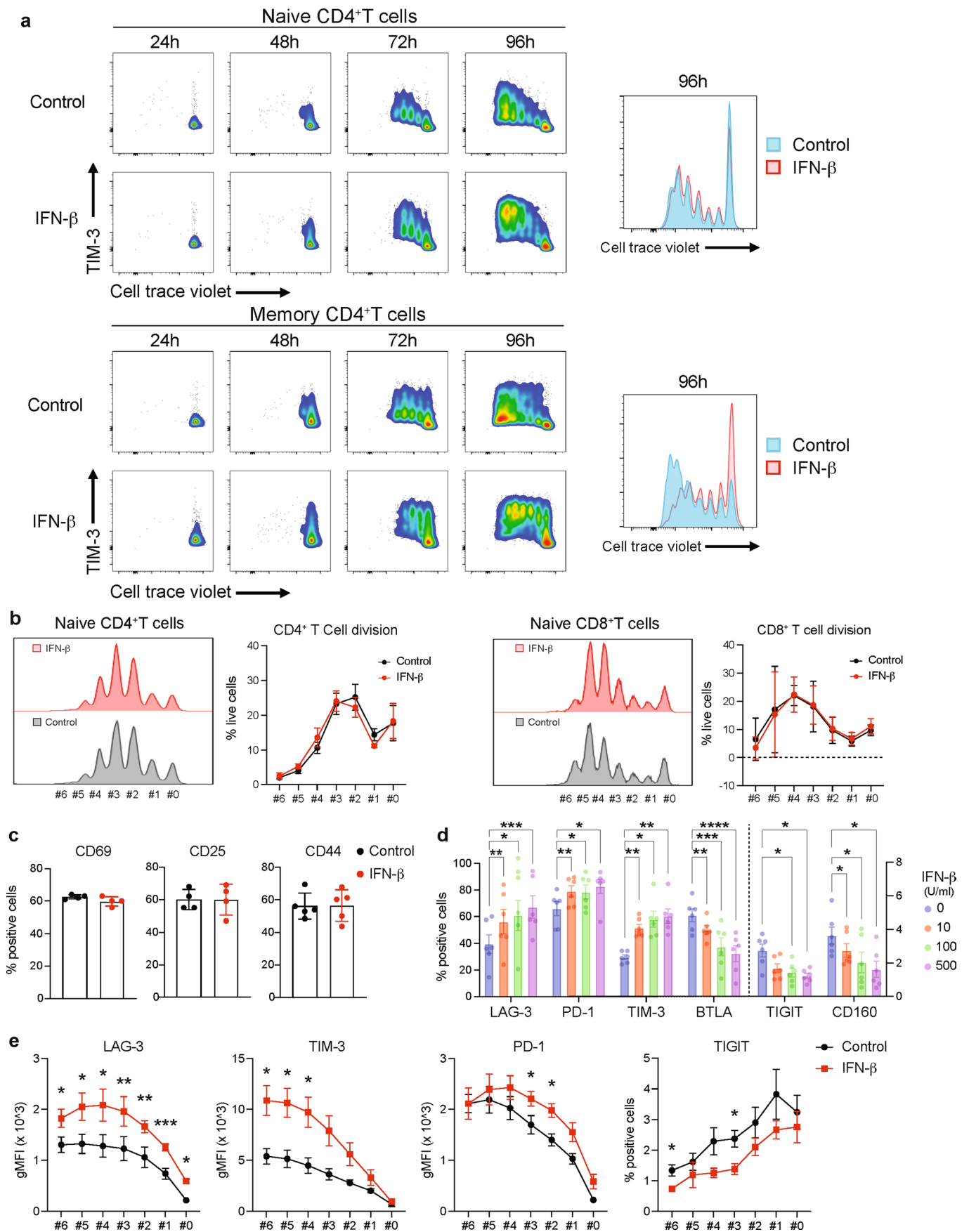


Extended Data Fig. 1 | FACS gating strategy for isolating naïve CD4⁺ and CD8⁺ T cells and schematic experimental workflow. Representative gating strategy for sorting naïve CD4⁺ and CD8⁺ T cells are shown. FACS isolated cells were immediately plated on 96 well round bottom plates coated with anti-CD3 (2 µg/ml) and soluble anti-CD28 (1 µg/ml) in the absence or presence of human IL-27 (100 ng/ml) or IFN-β (500 U/ml).



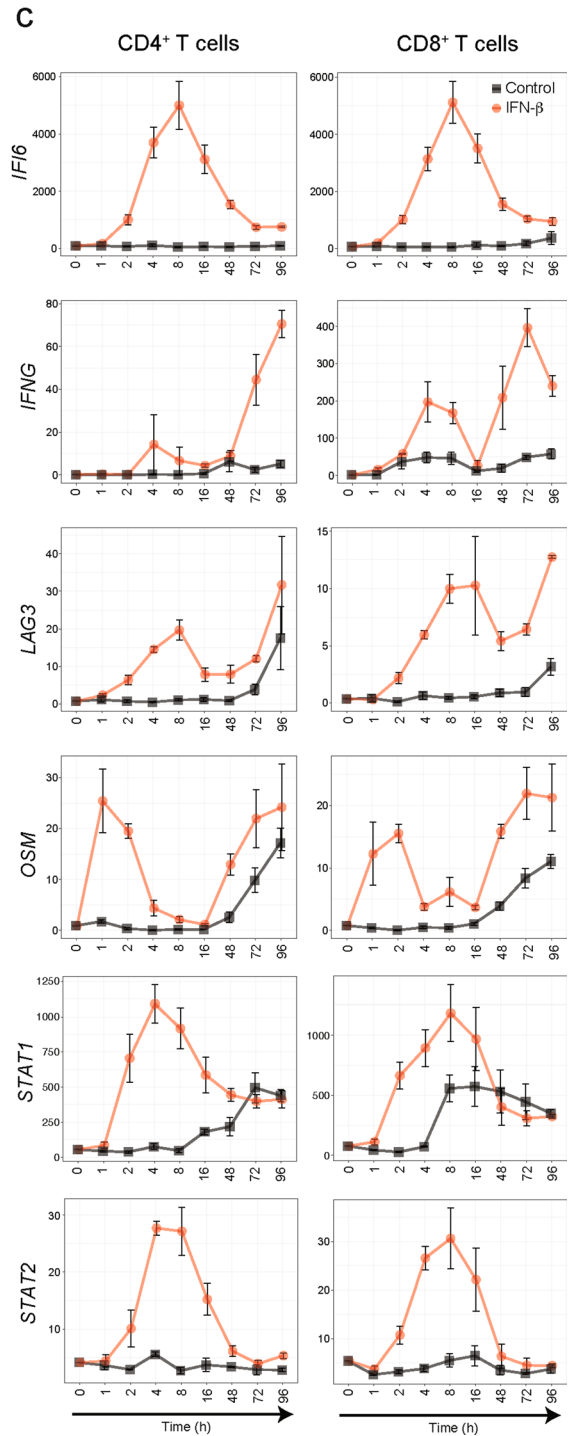
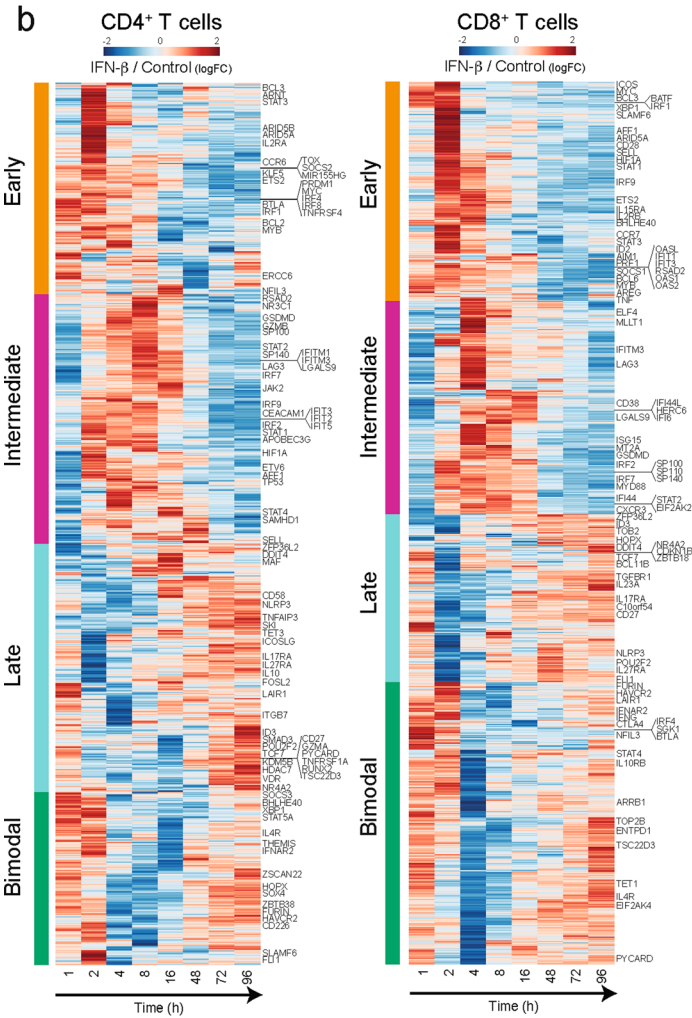
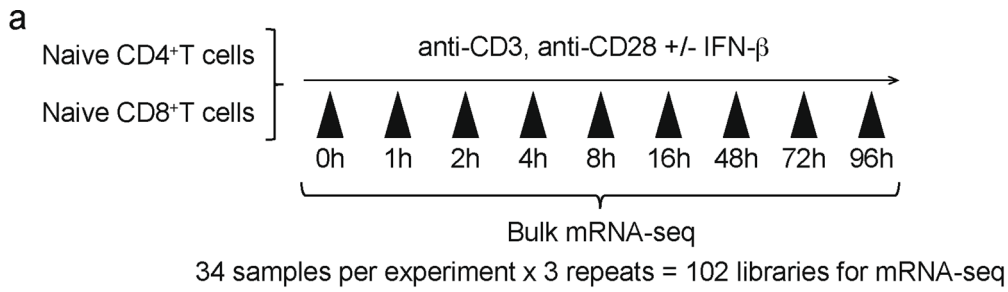
Extended Data Fig. 2 | See next page for caption.

Extended Data Fig. 2 | IFN- β differently regulates co-inhibitory receptors in human T cells. **a**, Representative histograms of surface expression of TIM-3, LAG-3, and PD-1 assessed by flow cytometry at 72-96 hours after stimulation. Dotted lines represent isotype control staining. Percent single positive cells for TIM-3, LAG-3, and PD-1 (middle) and triple positive cells (right) are shown ($n=6-8$; biologically independent samples). * $p < 0.05$, ** $p < 0.01$, **** $p < 0.0001$. **b**, Representative contour plots of flow cytometry analysis for TIM-3 and TIGIT expression in naïve CD4⁺ and CD8⁺ T cells (left). Cells were treated as Extended Data Fig. 1 and analyzed at 72 hours of culture. Percent TIGIT positive cells in naïve CD4⁺ T are shown ($n=8$; biologically independent samples). * $p < 0.05$, ** $p < 0.01$. (middle). qPCR analysis of *TIGIT* expression over the time course (13 time points from 0 to 96 hours). Each dot represents the average expression of two independent individuals' data. **** $p < 0.0001$. **c**, qPCR analysis of *IL10* and *IFNG* expression over the time course (13 time points from 0 to 96 hours). Each dot represents the average expression of two independent individuals' data (left). IL-10 and IFN- γ production assessed by intracellular staining (right). Cells are treated as in **a**, and cytokines are stained intracellularly. Cytokine positive cells are detected by flow cytometry ($n=6$; biologically independent samples). **d**, Representative contour plots of flow cytometry analysis for CD160 and BTLA expression and overlaid histogram for BTLA expression in naïve CD4⁺ and CD8⁺ T cells (left). Cells were treated as outlined in **b** and analyzed at 72 hours of culture. Percent positive cells for CD160 and BTLA in naïve CD4⁺ T are shown ($n=8$; biologically independent samples) (right). * $p < 0.05$, ** $p < 0.01$. Repeated-measures one-way ANOVA with Tukey's multiple comparisons test (**a-c**), and paired student's t-test (**d**).



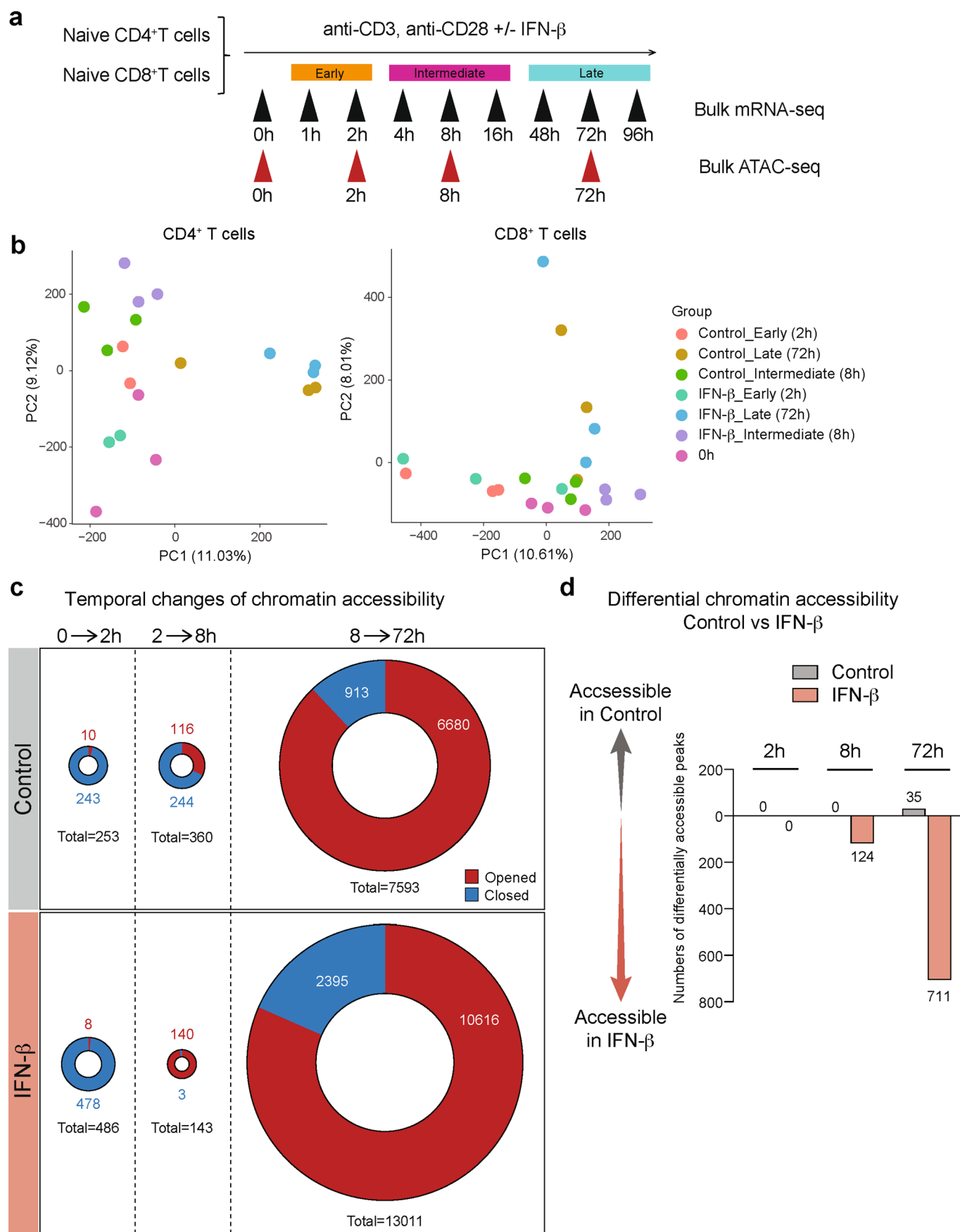
Extended Data Fig. 3 | See next page for caption.

Extended Data Fig. 3 | The impact of IFN- β on co-inhibitory receptors is not associated with T cell activation. **a**, Representative plots for T cell proliferation assay using cell trace violet dye. Naive and memory CD4⁺ T cells were stimulated with anti-CD3 and anti-CD28 in the absence or presence of IFN- β . TIM-3 expression and cellular proliferation were assessed at 24, 48, 72, and 96 hours after stimulation. Overlaid histogram for control and IFN- β condition were shown at right. **b**, Frequency of living cells at each cellular division state was calculated in naïve CD4⁺ T cells (left) and naïve CD8⁺ T cells (right) at 96 hours. There is no statistical difference observed between control vs IFN- β condition (n=5; biologically independent samples). **c**, T cell activation markers (CD44, CD25, CD69) were quantified by flow cytometry in naïve CD4⁺ T cells at 96 hours. There is no statistical difference observed between control vs IFN- β condition (n=4-5; biologically independent samples). **d**, Dose dependent effects of IFN- β on co-inhibitory receptors assessed by flow cytometry (n=6; biologically independent samples). *p < 0.05, **p < 0.01, ***p < 0.001, ****p < 0.0001. Two-way ANOVA with Dunnett's multiple comparisons test. **e**, LAG-3, PD-1, TIM-3, and TIGIT expressions were assessed by flow cytometry at each cellular division state (n=4; biologically independent samples). *p < 0.05, **p < 0.01, ***p < 0.001. Paired t test at each time point. Data was represented with mean \pm SEM.



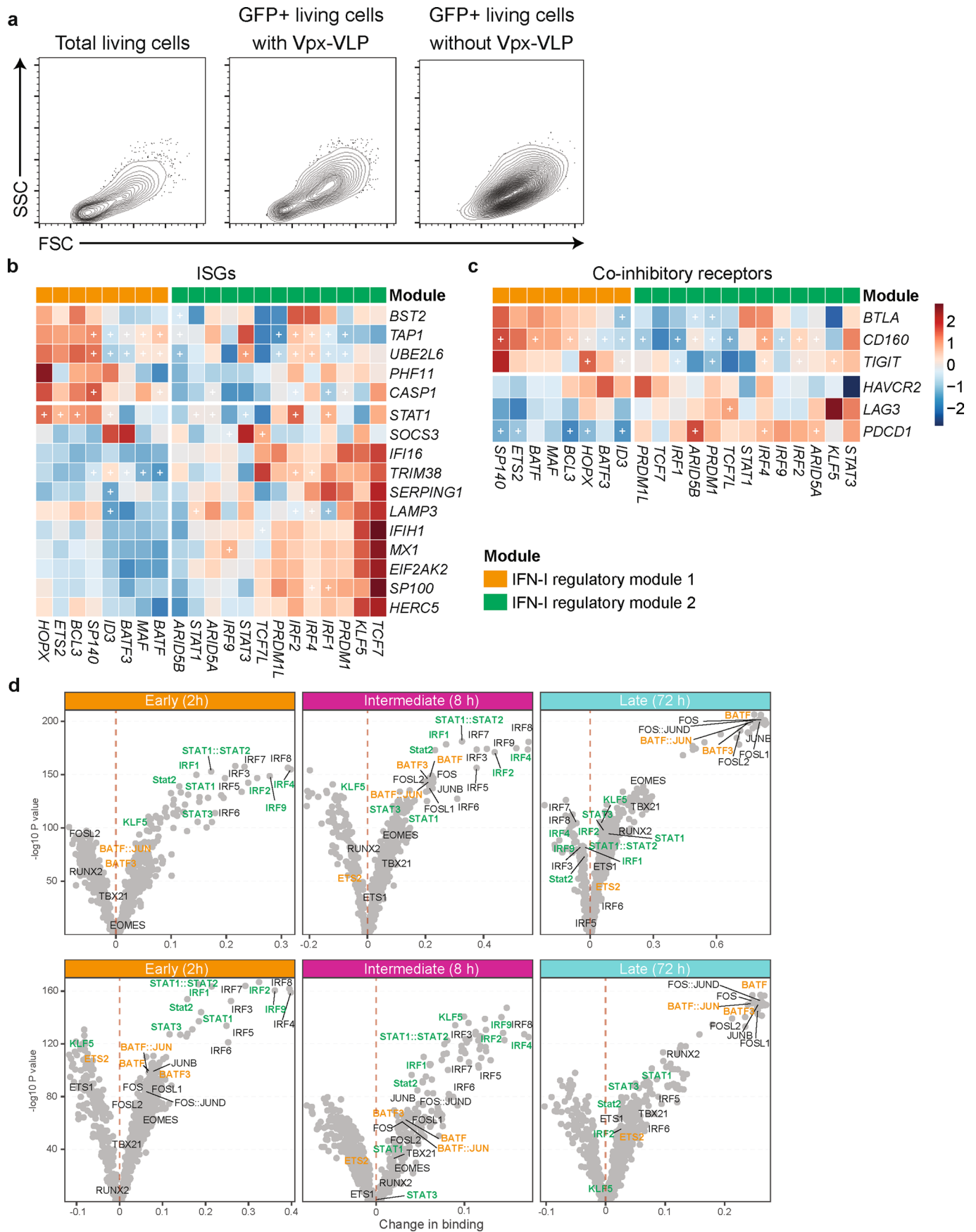
Extended Data Fig. 4 | See next page for caption.

Extended Data Fig. 4 | Dynamic transcriptomic changes by IFN- β in human T cells. **a**, Schematic experimental setup for high temporal resolution transcriptional profiling. **b**, Heatmap showing log fold change of DE gene expression between IFN- β and control Th0 condition at each timepoints for naive CD4⁺ (left) and CD8⁺ T cells (right). Genes are clustered based on the three transcriptional wave or bi-modal pattern. **c**, Line plots for *IFI6*, *IFNG*, *LAG3*, *OSM*, *STAT1*, and *STAT2* expression in naive CD4⁺ (left) and CD8⁺ T cells (right).



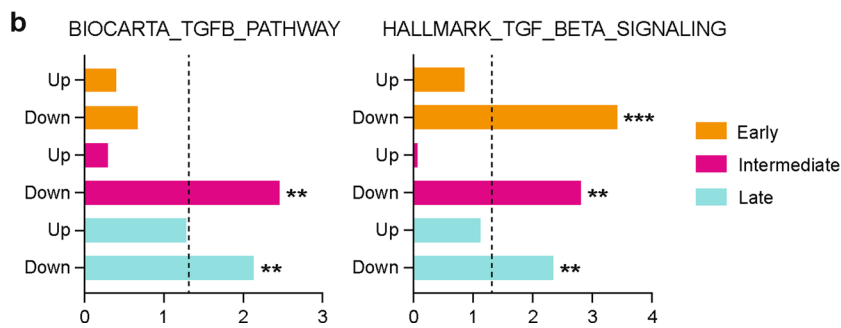
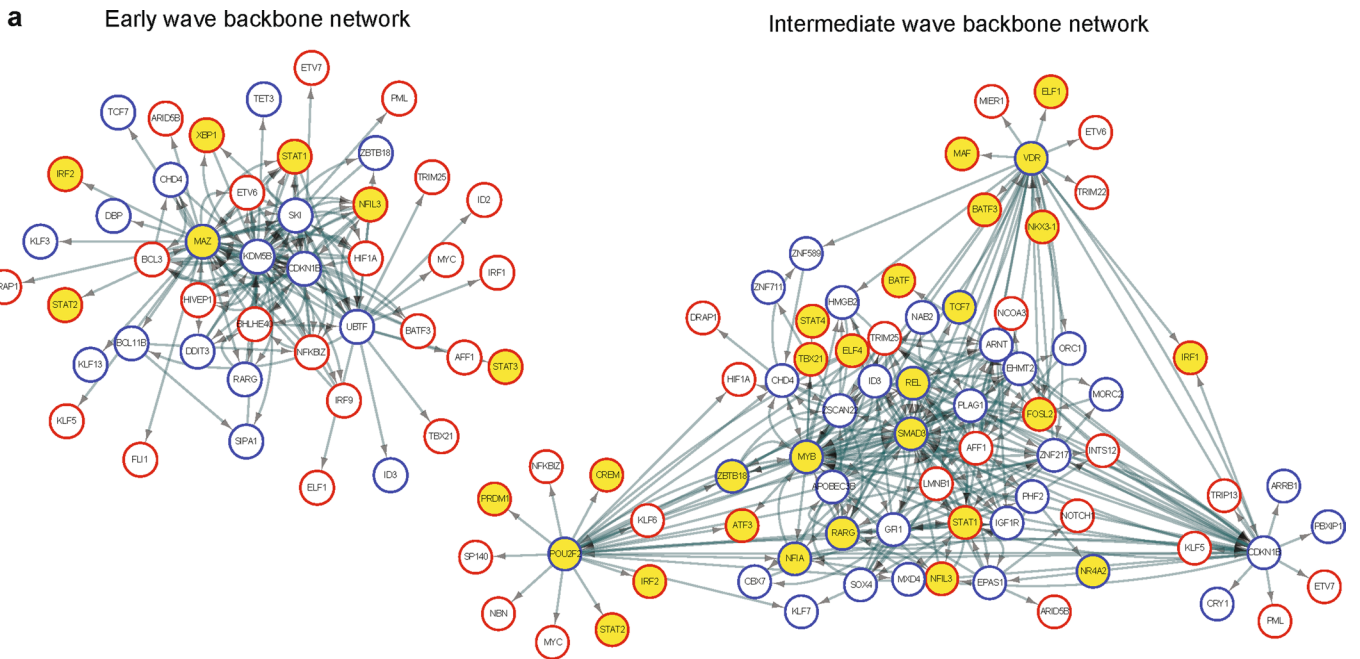
Extended Data Fig. 5 | See next page for caption.

Extended Data Fig. 5 | Dynamic changes of chromatin accessibility by IFN- β in human T cells. **a**, Schematic experimental setup for ATAC-seq experiment. **b**, PCA plots based on ATAC-seq peaks. Each dot represents one sample demonstrating the difference between the control and IFN- β groups, and the four different time points (0 h, 2 h, 8 h, 72 h). **c**, Pie charts depicting the differential chromatin accessibility between two time points, for both control and IFN- β treatment. The red or blue colored areas represent the numbers of opened or closed ATAC peaks compared to earlier time point, respectively. **d**, Bar plots describing the differential accessibility between IFN- β treatment and control at each time points.

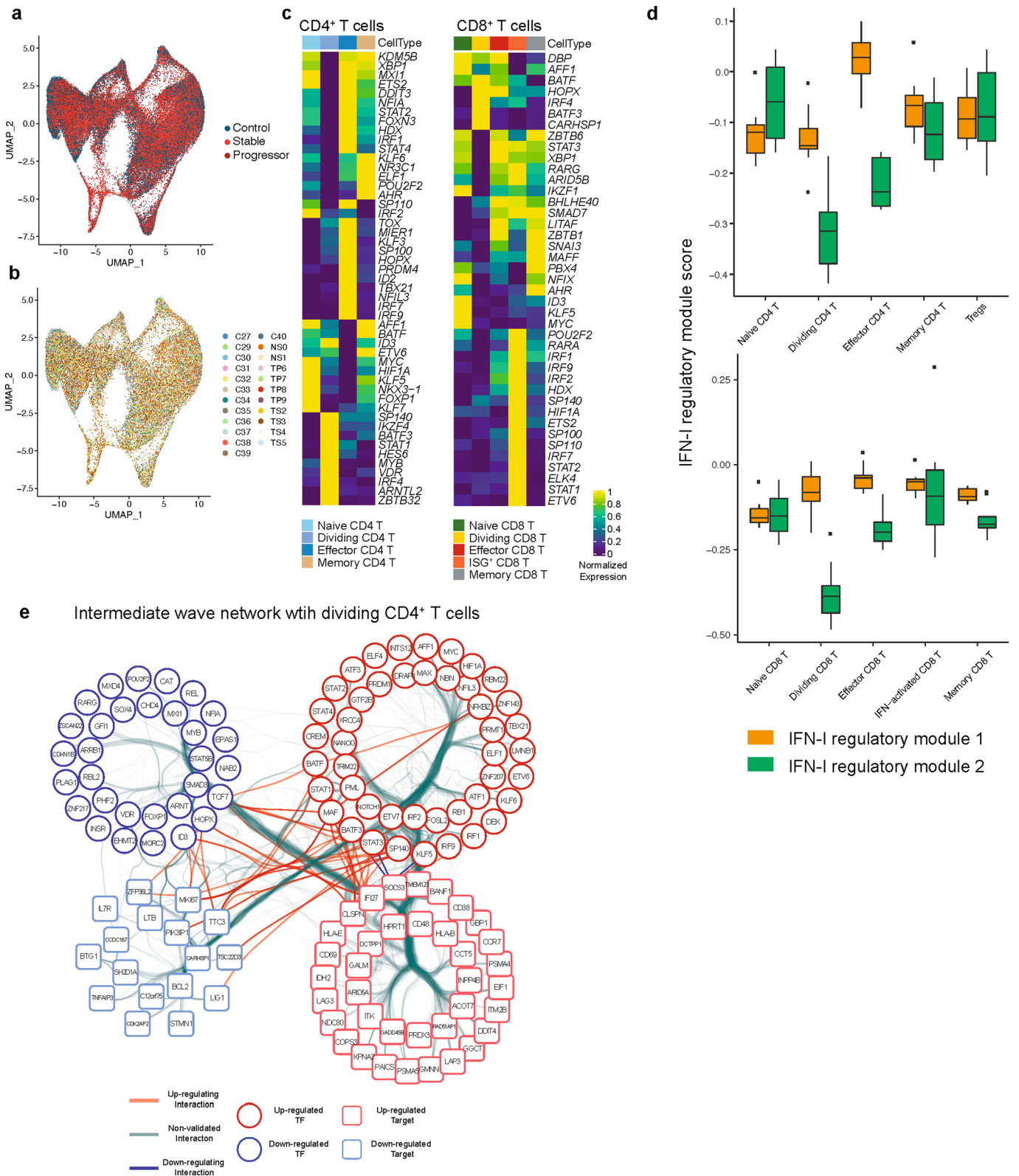


Extended Data Fig. 6 | See next page for caption.

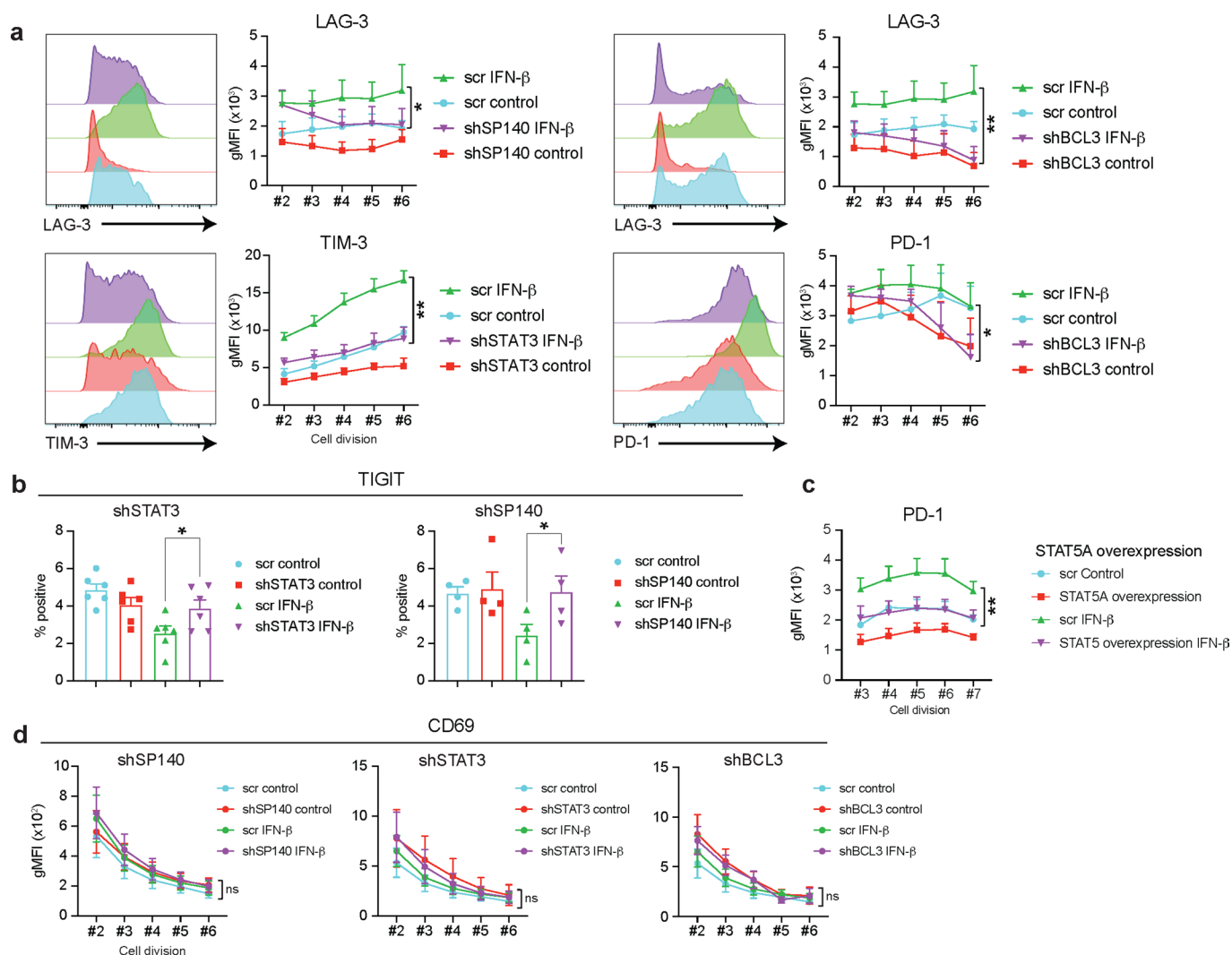
Extended Data Fig. 6 | Two IFN-I regulatory modules govern both transcriptional and epigenetic changes during IFN-I response. **a**, Contour plots for total living cells and backgating analysis for GFP positive cells. Primary naïve CD4⁺ T cells were transduced with scramble shRNA control LV with or without Vpx-VLPs pre-transduction. Cells are collected at 96 hours after starting stimulation and analyzed by flow cytometry. **b, c**, Heatmaps showing the effect of TFs perturbation under IFN- β stimulation on ISGs (**b**) and co-inhibitory receptors (**c**). Values in the heatmap were normalized by subtractions of log₁₀ fold change of scramble shRNA control over perturbed expression. The '+' sign indicates a statistically significant effect with an adjusted P.value < 0.05 (details in Methods). **d**, Volcano plots depicting differential TF binding activity against the $-\log_{10}(p \text{ value})$ (both provided by TOBIAS) of all investigated TF motifs; each dot represents one motif. Positive binding activity represents more enrichment in IFN- β treatment compared to control. The motifs for IFN-I regulator module 1 and IFN-I regulator module 2 were highlighted in orange and green, respectively.



Extended Data Fig. 7 | Backbone network analysis identify downregulated TGF- β signature during IFN- β response. a, Directed TF backbone networks at the early and intermediate waves. The regulation and interaction of each DETFs at each transcriptional wave were depicted. TF footprints enriched in IFN- β condition were highlighted in yellow. **b**, ssGSEA for TGF- β signaling pathways with upregulated TFs (Up) and downregulated TFs (Down) at each transcriptional wave. Adjusted p values are shown and the dotted line indicates a threshold of significance defined by adjusted p value = 0.05. ** $p < 0.01$, *** $p < 0.001$. Data was represented with mean \pm SEM.



Extended Data Fig. 8 | IFN-I regulator expression profiles in T cells from COVID-19. **a, b**, UMAP representation of T cells from healthy control samples (n = 13; biologically independent samples) and COVID-19 samples (n = 18; biologically independent samples) color coded by **a**, disease conditions and **b**, each individual. Cells from the same individual were labeled as one subject code, which resulted in 10 individual codes shown in **b, c**. Heatmap showing the expression of DETFs for CD4⁺ and CD8⁺ T cells in each T cell subset. **d**, IFN-I regulator module 1 and 2 scores for CD4⁺ and CD8⁺ T cells across sub cell types. **e**, Bundled regulatory network showing interactions between regulators at intermediate phase and transcriptional signature of dividing CD4⁺ T cells in COVID-19. Regulators at the intermediate phase are marked with circles (red; upregulated TFs, blue; downregulated TFs), and genes that are differentially expressed in dividing CD4⁺ T cells in COVID-19 were marked with squares (light red; upregulated DEGs, light blue; downregulated DEGs).



Extended Data Fig. 9 | Validation of key IFN-I regulators controlling co-inhibitory receptors in human T cells. a, Co-inhibitory receptor expression was assessed at each cellular division state (division #2-6) under each TF gene knockdown performed as well as in Fig. 3. The effects of each gene perturbation over GFP control vector (GFP) treated with IFN- β were determined by repeated-measures two-way ANOVA with Fisher's LSD test. The statistical significance between GFP control vector with IFN- β (GFP + IFN- β) vs gene knockdown with IFN- β (shRNA + IFN- β) condition was shown. * $p < 0.05$, ** $p < 0.01$. **b**, Frequency of TIGIT positive cells was determined in perturbation for SP140 and STAT3 ($n = 4$; biologically independent samples). * $p < 0.05$. **c**, STAT5A was overexpressed on human primary naïve CD4⁺ T cells and PD-1 expression was shown at each cellular division state (division #3-7). Repeated-measures two-way ANOVA with Fisher's LSD test was applied and the comparison between GFP control vector with IFN- β (GFP + IFN- β) vs STAT5A overexpression with IFN- β (STAT5A overexpression + IFN- β) condition was shown ($n = 6$; biologically independent samples). ** $p < 0.01$. **d**, CD69 expression was assessed at each cellular division state with three TF perturbation experiments (SP140, STAT3, and BCL3) ($n = 4$; biologically independent samples). Statistics were determined as well as in **a**. ns; not significant. Data was represented with mean \pm SEM.

Reporting Summary

Nature Research wishes to improve the reproducibility of the work that we publish. This form provides structure for consistency and transparency in reporting. For further information on Nature Research policies, see our [Editorial Policies](#) and the [Editorial Policy Checklist](#).

Statistics

For all statistical analyses, confirm that the following items are present in the figure legend, table legend, main text, or Methods section.

n/a Confirmed

- The exact sample size (n) for each experimental group/condition, given as a discrete number and unit of measurement
- A statement on whether measurements were taken from distinct samples or whether the same sample was measured repeatedly
- The statistical test(s) used AND whether they are one- or two-sided
Only common tests should be described solely by name; describe more complex techniques in the Methods section.
- A description of all covariates tested
- A description of any assumptions or corrections, such as tests of normality and adjustment for multiple comparisons
- A full description of the statistical parameters including central tendency (e.g. means) or other basic estimates (e.g. regression coefficient) AND variation (e.g. standard deviation) or associated estimates of uncertainty (e.g. confidence intervals)
- For null hypothesis testing, the test statistic (e.g. F , t , r) with confidence intervals, effect sizes, degrees of freedom and P value noted
Give P values as exact values whenever suitable.
- For Bayesian analysis, information on the choice of priors and Markov chain Monte Carlo settings
- For hierarchical and complex designs, identification of the appropriate level for tests and full reporting of outcomes
- Estimates of effect sizes (e.g. Cohen's d , Pearson's r), indicating how they were calculated

Our web collection on [statistics for biologists](#) contains articles on many of the points above.

Software and code

Policy information about [availability of computer code](#)

Data collection Flow cytometry data were collected using a LSR Fortessa with FACSDiva Software Version 8.0.1 (BD Pharmingen).

Data analysis FACS: Flow Cytometry Standard (FCS) 3.0 files were analyzed with FlowJo 10 (FlowJo LLC).
Gene expression data analysis:
The software used for the analyses of each of the data platforms and integrated analyses are described and referenced in the individual Method Details subsections.
List all software versions used:
R:
R 4.1.1 <https://www.r-project.org/>
Rstudio 4.1.1 <https://rstudio.com/>
DESeq2 package <http://bioconductor.org/packages/release/bioc/html/DESeq2.html>
GGplot2 package <https://ggplot2.tidyverse.org/reference/ggplot.html>
Pheatmap package <https://cran.r-project.org/web/packages/pheatmap/pheatmap.pdf>
Dendsort package <https://cran.r-project.org/web/packages/dendsort/dendsort.pdf>
dplyr <https://cran.r-project.org/web/packages/dplyr/vignettes/dplyr.html>
Seurat <https://cran.r-project.org/web/packages/Seurat/Seurat.pdf>
Matrix <https://cran.r-project.org/web/packages/Matrix/Matrix.pdf>
tidyr <https://cran.r-project.org/web/packages/tidyr/tidyr.pdf>
ComplexHeatmap <http://bioconductor.org/packages/release/bioc/manuals/ComplexHeatmap/man/ComplexHeatmap.pdf>
TOBIAS <https://github.com/loosolab/TOBIAS>
MACS2 <https://github.com/topics/mac2>
FastQC <https://www.bioinformatics.babraham.ac.uk/projects/fastqc/>
Picard <http://broadinstitute.github.io/picard/>

ataqv <https://github.com/ParkerLab/ataqv>

Trimmomatic V0.32 http://www.usadellab.org/cms/uploads/supplementary/Trimmomatic/TrimmomaticManual_V0.32.pdf

Python:

Python 3.7 <https://www.python.org/>

Spyder 4 <https://www.spyder-ide.org/>

Pandas package <https://pandas.pydata.org/>

Numpy package <https://numpy.org/>

Scipy package <https://www.scipy.org/>

Seaborn package <https://seaborn.pydata.org/>

Matplotlib package <https://matplotlib.org/>

Networkx package <https://networkx.org/>

Cytoscape:

cytoscape 3.8 <https://cytoscape.org/>

yFiles Layout Algorithms package <https://www.yworks.com/products/yfiles-layout-algorithms-for-cytoscape>

For manuscripts utilizing custom algorithms or software that are central to the research but not yet described in published literature, software must be made available to editors and reviewers. We strongly encourage code deposition in a community repository (e.g. GitHub). See the Nature Research [guidelines for submitting code & software](#) for further information.

Data

Policy information about [availability of data](#)

All manuscripts must include a [data availability statement](#). This statement should provide the following information, where applicable:

- Accession codes, unique identifiers, or web links for publicly available datasets
- A list of figures that have associated raw data
- A description of any restrictions on data availability

The raw sequencing data is available through GSE195543.

Field-specific reporting

Please select the one below that is the best fit for your research. If you are not sure, read the appropriate sections before making your selection.

Life sciences Behavioural & social sciences Ecological, evolutionary & environmental sciences

For a reference copy of the document with all sections, see nature.com/documents/nr-reporting-summary-flat.pdf

Life sciences study design

All studies must disclose on these points even when the disclosure is negative.

Sample size	No formal sample size power calculation was performed. Sample sizes were determined by the previous reports from our groups and the others. The number of subjects in each experiments were indicated in each figure legend.
Data exclusions	For perturbation mRNA-seq data, one sample from shSTAT1 in control condition and another sample from shSTAT3 in control condition were excluded because of obvious sequencing batch effect.
Replication	For bulk mRNA-seq based high resolution transcriptional profiling and ATAC-seq based chromatin accessibility profiling, we repeated three times of independent experiment with using the same donor's T cells. The results are replicated with the other experiments using RNA-seq and validated by qPCR. For perturbation experiment with bulk mRNA-seq, we performed one times with three technical replicates, but the key findings were repeated by the other donor at least another independent experiment. In validation experiment at the level of proteins, we performed more than four biological replicates (individuals) with more than three independent experimental repeats. All the other data were reliably reproduced in at least two independent experiments.
Randomization	Healthy control subjects were randomly selected in order to avoid potential biases . No manual randomization was performed on these samples.
Blinding	Since there is no subjective measurement involved, no-blinding is necessary.

Reporting for specific materials, systems and methods

We require information from authors about some types of materials, experimental systems and methods used in many studies. Here, indicate whether each material, system or method listed is relevant to your study. If you are not sure if a list item applies to your research, read the appropriate section before selecting a response.

Materials & experimental systems

Methods

- n/a Involved in the study
- Antibodies
- Eukaryotic cell lines
- Palaeontology and archaeology
- Animals and other organisms
- Human research participants
- Clinical data
- Dual use research of concern

- n/a Involved in the study
- ChIP-seq
- Flow cytometry
- MRI-based neuroimaging

Antibodies

Antibodies used

Antigen/Clone/Fluorophore/Supplier/Dilution/Product#
 TIM-3/(7D3)/PE-CF594/(BD Pharmingen)/1:100/565560
 CD279 (PD-1)/(EH12.1)/PE-Cy7/(BD Pharmingen)/1:100/561272
 CD4/(RPA-T4)/V450/(BD Pharmingen)/1:100/560345
 CD8/(RPA-T8)/FITC/(BD Pharmingen)/1:100/557085
 CD25/(2A3)/PE/(BD Pharmingen)/1.25/341010
 CD25/(2A3)/PE-Cy7/(BD Pharmingen)/1:100/335807
 CD45RO/(UCHL1)/PE-Cy7/(BD Pharmingen)/1:100/560608
 CD45RA/(HI100)/APC-H7/(BD Pharmingen)/1:100/560674
 CD127/(hIL-7R-M21)/Alexa647/(BD Pharmingen)/1.25/558598
 LAG-3/(11C3C65)/PE/(BioLegend)/1:100/369306
 LAG-3/(11C3C65)/Brilliant Violet 421/(BioLegend)/1:100/369314
 TIM-3/(F38-2E2)/APC/(BioLegend)/1:100/345012
 TIM-3/(F38-2E2)/Brilliant Violet 650/(BioLegend)/1:100/345028
 TIGIT/(A15153G)/APC/(BioLegend)/1:100/372706
 TIGIT/(A15153G)/Biotinylated/(BioLegend)/1:100/372722
 TIGIT/(A15153G)/PE-Cy7/(BioLegend)/1:100/372714
 IL-10/(JES3-9D7)/PE/(BioLegend)/1:100/501404
 BTLA/(MIH26)/PE-Cy7/(BioLegend)/1:100/344516
 CD160/(BY55)/PE/(BioLegend)/1:100/341206
 CD44/(IM7)/Brilliant Violet 650/(BioLegend)/1:100/103049
 CD69/(FN50)/PE-Cy7/(BioLegend)/1:100/310912
 Streptavidin/Brilliant Violet 650/(BioLegend)/1:1000/405232
 IFN-gamma/(4S.B3)/PE-Cy7/(eBioscience)/1:100/25-7319-82
 All information is available in Supplementary Table 3.

Validation

All antibodies are reactive against human and have been validated by the manufacturer by flow cytometric analysis.

Eukaryotic cell lines

Policy information about [cell lines](#)

Cell line source(s) Lenti-X™ 293T Cell Line were purchased from Takara Bio.

Authentication No authentication performed.

Mycoplasma contamination Not tested for mycoplasma contamination.

Commonly misidentified lines (See [ICLAC](#) register) No commonly misidentified cell lines used.

Human research participants

Policy information about [studies involving human research participants](#)

Population characteristics Healthy subjects (female or male between the ages of 27 and 50) were randomly selected.

Recruitment Healthy donors were recruited by International Review Board (IRB)-approved study, and written consent was obtained.

Ethics oversight Research protocol was reviewed and approved by the Yale Human Research Protection Program Institutional Review Boards (FWA00002571, Protocol ID. 2000027291).

Note that full information on the approval of the study protocol must also be provided in the manuscript.

Plots

Confirm that:

- The axis labels state the marker and fluorochrome used (e.g. CD4-FITC).
- The axis scales are clearly visible. Include numbers along axes only for bottom left plot of group (a 'group' is an analysis of identical markers).
- All plots are contour plots with outliers or pseudocolor plots.
- A numerical value for number of cells or percentage (with statistics) is provided.

Methodology

Sample preparation

Single-cell suspensions were prepared from human PBMCs. Total T cells were isolated by negative selection using human T cell isolation kit (Stemcell). Cells were stained with fixable viability dye in PBS for 10 min at RT, followed by staining with surface antibodies in 2% FBS + 1mM EDTA containing PBS for 30 min at 4°C. For intracellular staining, cells were fixed and permeabilized with the Foxp3 Fix/Perm buffer set (eBioscience) for 1 hr at 4°C, followed by staining with intracellular antibodies. For cytokine staining, cells were stimulated with PMA/ionomycin in the presence of GolgiPlug (BD Bioscience) for 4 hr at 37°C, followed by intracellular staining method.

Instrument

BD FACSAriaII, BD Fortessa

Software

BD FACSDIVA, BD Flowjo

Cell population abundance

The sort purity was over 95%.

Gating strategy

The cells were firstly gated on a size using SSC/FSC, then on a single cell gate based on FSC-H/FSC-W and SSC-H/SSC-W. Live cells are gated on fixable live dead cell staining negative population. All the gates subsequent to live cells are shown in the supplementary figure 1.

- Tick this box to confirm that a figure exemplifying the gating strategy is provided in the Supplementary Information.